Spring 5-15-2015

Gold Nanostructures for Sensing and Functional Bioimaging

Maximilian Y. Fei
Washington University in St Louis

WASHINGTON UNIVERSITY IN SAINT LOUIS
School of Engineering and Applied Science
Department of Mechanical Engineering and Material Science

Thesis Examination Committee:
Srikanth Singamaneni
Parag Banerjee
Jerry Morrissey

Gold Nanostructures for Sensing and Functional Bioimaging

By
Maximilian You Fei

A thesis presented to the School of Engineering
of Washington University in partial fulfillment of the
requirements for the degree of Master of Science

May 2015

Saint Louis, Missouri

Contents

List of Figures

Acknowledgments

I would first like to thank Professor Srikanth Singamaneni and Dr. Limei Tian for giving me the opportunity to contribute to the Soft Nanomaterials Laboratory at Washington University in Saint Louis. Their support, coupled with their experience and expertise, has been instrumental to my academic success.

A special thanks goes out to the Office of Congressionally Directed Medical Research Programs (DoD-Army contract number W81XWH-11-1-0439). I would also like to express my gratitude for financial support from a NSF CAREER award (CBET-1254399) and the BRIGHT Institute at Washington University in Saint Louis under the P50 Pilot Project Program.

I am also grateful to the graduate students, faculty, and staff in the MEMS department that have helped me through this process.

Maximilian You Fei

Washington University in Saint Louis
May 2015

Dedicated to my family for their unwavering support.

ABSTRACT

Gold Nanostructures for Sensing and Functional Bioimaging

by

Maximilian You Fei

Master of Science in Materials Science and Engineering

Washington University in Saint Louis, 2015

Research Advisor: Professor Srikanth Singamaneni

Gold nanostructures offer an extremely promising path forward in the fields of imaging and sensing because of their unique optical and chemical properties. Here, we demonstrate that plasmonic nanostructures can be employed as nanoscale transducers to monitor the growth and phase transitions in ultrathin polymer films. In particular, gold nanorods with high refractive index sensitivity (~150 nm / refractive index unit (RIU)) were employed to probe the growth and swelling of polyelectrolyte multilayers (PEM). By comparing the wavelength shift and extinction intensity of the localized surface plasmon resonance (LSPR) of the gold nanorods coated with PEM in air and water, the swelling of PEM was estimated to be 26%±6%, which was confirmed with atomic force microscope (AFM) imaging in air and water. The deployment of shape-controlled metal nanostructures with high refractive index sensitivity represents a novel and facile approach for monitoring the phase transition in polymers with nanoscale resolution.

Additionally, we demonstrate bio-enabled synthesis of a novel class of functional surface enhanced Raman scattering (SERS) probes with built-in and accessible electromagnetic hotspots, which are formed by densely packed satellites grown on a gold plasmonic core. These accessible electromagnetic hotspots enable facile sampling of the surrounding complex biological milieu. The core-satellite superstructures serve as nanoscale sensors to spatiotemporally map intravesicular pH changes along endocytic pathways inside a living cell. Furthermore, we show that through rational choice of core shape, photothermal efficiency of the nanostructures can be modulated to realize either of the following: imaging probes with minimal heating, or multifunctional theranostic agents that can image and photothermally kill the cells for locoregional therapy. Bright, stable and multifunctional exogenous contrast agents are critical for advancing SERS-based functional bioimaging and image-guided therapy.

Chapter 1

Background

1.1 Localized Surface Plasmon Resonance

From an electromagnetic (EM) point of view, metals can be considered plasmas composed of fixed positive ion cores with mobile conduction electrons. When an EM wave (comprised of an oscillating electric field) interacts with a metal, free electrons begin collectively and coherently oscillating at the plasma frequency. These oscillations of the free electron density against the fixed positive ions in the metal are known as plasmons. Excitation of localized surface plasmons results in strong light scattering and absorption when the plasmon frequency is in resonance with the incident wavelength. The frequency and intensity of the surface plasmon absorption bands are highly sensitive to the size and shape of the nanostructures, as well as to the surrounding dielectric environment, producing bright colors when nanoparticles are suspended in solution. The sensitivity of LSPR to local changes in the dielectric environment renders it an attractive transduction platform for chemical and biological sensing. LSPR of metal nanostructures has been shown to be sensitive enough to differentiate inert gases with refractive index contrast on the order of 3×10^{-4}, probe the conformational changes of biomacromolecules, detect single biomolecule binding events, monitor the kinetics of catalytic activity of single nanoparticles, and even optically detect single electrons. One area in particular that plasmonics is expected to make an enormous impact is the field of life sciences, with applications in high-contrast imaging and non/minimally-invasive diagnostics and therapeutics. [1]

1.2 Surface Enhanced Raman Scattering

One particularly important manifestation of LSPR is Raman scattering, which is an optical phenomenon wherein incident photons interact with a molecule upon contact in such a way that energy is either gained or lost, resulting in inelastic scattering of the photon. This phenomenon yields a molecular "fingerprint," making Raman spectroscopy well-suited for identification and characterization of unknown analytes. This technique is particularly advantageous because it (i) does not suffer from interferences from water, (ii) requires little to no sample preparation, (iii) is robust and

can be used in numerous environments, (iv) is relatively insensitive to the wavelength of excitation employed, and (v) produces a narrow-band spectral signature unique to the molecular vibrations of the analyte. However, Raman spectroscopy has remained a marginalized technique, primarily due to the extremely low scattering cross sections. SERS overcomes this shortcoming by utilizing the intense EM fields surrounding metal nanostructures to magnify the signal from Raman scattering by 6 to 8 orders of magnitude. Under ideal conditions, this enhancement is capable of detecting the presence of a single molecule. Because of the myriad of opportunities presented by SERS, there exists a strong demand for SERS probes that are highly sensitive, robust in different environments, and facile to synthesize. [2]

Chapter 2

Au Nanorods for Monitoring Growth and Swelling of Ultra-Thin Polymer Films

2.1 Introduction

The LSPR wavelength of metal nanostructures is sensitive to numerous factors, including the composition, size, shape, dielectric medium and proximity to other nanostructures (plasmon coupling). [3] The sensitivity of LSPR wavelength to localized changes in dielectric medium renders it an attractive transduction platform for chemical and biological sensing. [4, 5, 6, 7, 8, 9] LSPR has been shown to be sensitive enough for numerous applications, including differentiating various inert gases with a refractive index difference on the order of 3×10^{-4} RIU, probing the conformational changes of individual biomacromolecules, detecting single biomolecule binding events, monitoring the kinetics of catalytic activity of single NPs, and even optically detecting single electrons. [10, 11, 12, 13] While the swelling and shrinking of responsive polymers in response to external stimuli such as pH, temperature, and solvent quality has been employed to achieve responsive plasmonics (enabling tunable optical properties) [14, 15, 16, 17, 18, 19], the application of plasmonic nanostructures to quantitatively follow the phase transition (swelling-shrinking) in polymers is rare. [20]

Layer-by-layer (LbL) assembly of PEM involves alternating adsorption of oppositely charged polyelectrolytes. LbL assembly offers excellent control over the thickness of the PEM down to ~ 1nm. [21, 22] The thickness, internal structure, and surface roughness of PEM are sensitive to various parameters such as pH, ionic strength, polymer concentration, temperature, and humidity. [23, 24, 25, 26] The potential applications of such polymer films and microcapsules in porous membranes, responsive surfaces and interfaces, tissue engineering scaffolds, and controlled drug delivery vehicles are under extensive investigation. [27, 28, 29] In many of these applications, water transport plays an important role, necessitating a thorough understanding of the conformation and behavior of PEM in aqueous environments. Previous reports discussing the swelling behavior of PEM are primarily based on ellipsometry, propagating surface plasmon resonance (SPR) and AFM, both of which are time-

intensive methods of data acquisition and interpretation, and, in some cases, not suitable for real-time monitoring. [23, 30, 31, 32]

Here, we report gold nanorods (AuNRs) as plasmonic transducers to monitor the growth and swelling behavior of PEM. Although propagating SPR exhibits higher refractive index sensitivity and figure of merit (refractive index sensitivity/full width at half maximum of the SPR) compared to LSPR, the much smaller (nearly ten times) electromagnetic decay length of the LSPR, as compared to that in SPR, results in higher "surface sensitivity" to LSPR. [33] Thus, LSPR serves as an ideal platform to monitor the adsorption of ultrathin polymer films (i.e., thickness smaller than 30 nm). Furthermore, compared to propagating SPR, LSPR offers distinct advantages such as simplicity in detection, high spatial resolution down to single nanoparticle, and facile integration with device platforms.

2.2 Sample Preparation

Due to their high refractive index sensitivity (~150 nm/ RIU), gold nanorods were employed as plasmonic nanotransducers for probing the swelling of polyelectrolyte bilayers. The AuNR, synthesized using a seed-mediated approach, [34, 35] are positively charged with a length of ~54 nm and a diameter of ~20 nm (TEM image in Fig. 2.1A). The extinction spectrum of AuNR solution shows the characteristic transverse (515 nm) and longitudinal (667 nm) surface plasmon resonances of AuNR associated with the oscillation of conduction electrons in transverse and longitudinal directions of the nanorods (Fig. 2.1B).

AuNR were adsorbed on poly(2-vinyl pyridine) (P2VP)-modified glass slides by exposing the glass slide to AuNR solution, followed by extensive rinsing with water to remove the weakly adsorbed nanorods. The pyridyl groups of P2VP are known to have a high affinity to gold, resulting in strong adsorption of AuNR to P2VP film. [18, 36] Adsorption of AuNRs on a P2VP-modified glass substrate resulted in a blue shift in both transverse and longitudinal plasmon resonance wavelength (Fig. 2.1B). The blue shift in LSPR wavelength is due to the effective decrease in refractive index experienced by the AuNR on a substrate (substrate+air), as compared to water. The transverse plasmon exhibited a significantly smaller blue shift (~6 nm) compared to that of the longitudinal plasmon band (33 nm), which can be attributed to the higher refractive index sensitivity of the longitudinal plasmon band, relative to that of the transverse band. [37]

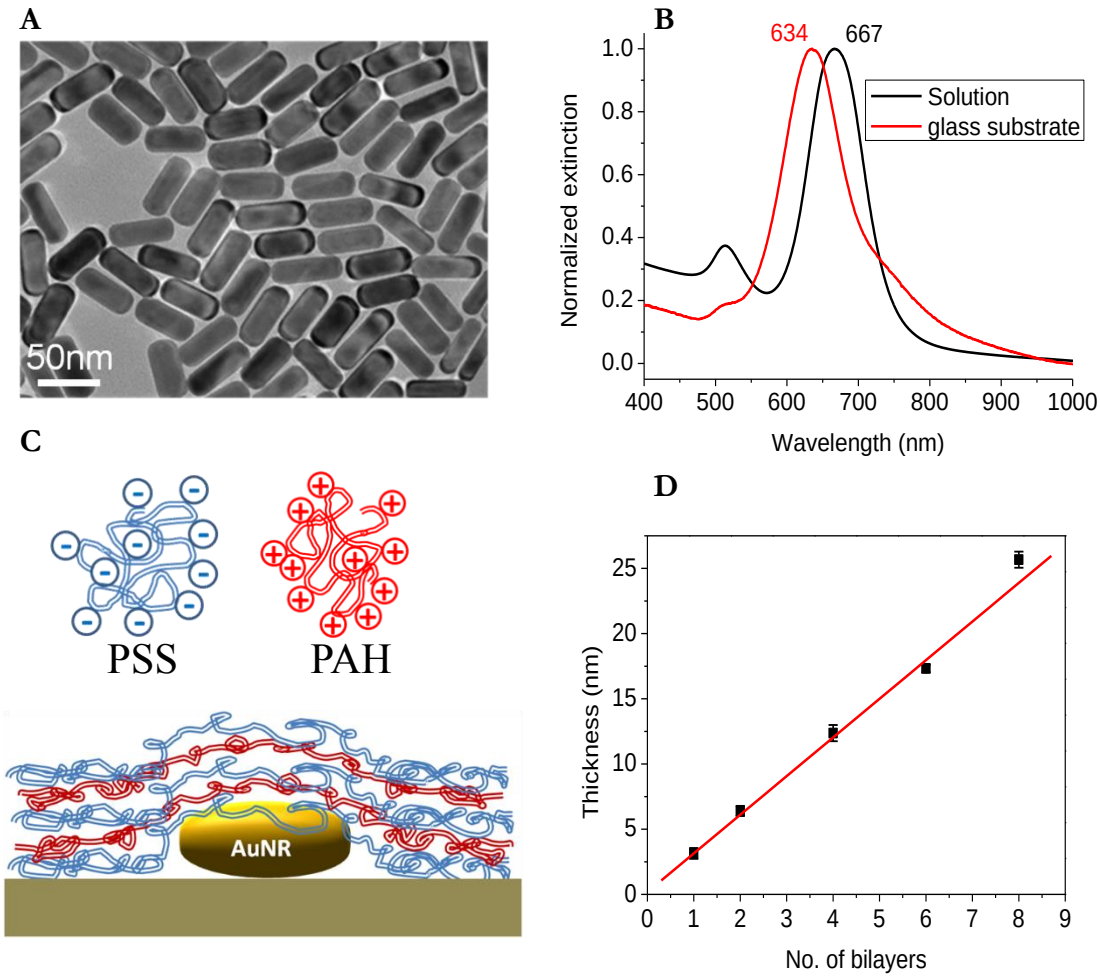

Figure 2.1 - (A) TEM image of gold nanorods (AuNRs) (B) UV-vis spectra of AuNRs in solution and on glass surface (C) schematic of ultrathin polymer layers deposited on AuNRs adsorbed on glass substrate, (D) plot showing the linear increase in the thickness of UPL with the increasing number of bilayers on silicon substrates.

PEM were formed on AuNR by alternate adsorption of negatively charged poly(styrene sulfonate) (PSS) and positively charged poly(allylamine hydrochloride) (PAH), using spin-assisted LbL assembly as described in the methods section (Fig. 2.1C). AFM scratch test measurements confirmed the expected linear growth of PEM thickness as a function of the number of bilayers. The average bilayer thickness was measured to be ~3 nm, which closely agreed with the values reported previously for PAH-PSS system (Fig. 2.1D). [38]

Numerous studies in the past have shown that PEM exhibit smooth and uniform morphology on planar surfaces. [26, 39, 40] However, in our study, PEM were deposited on AuNR adsorbed on a glass surface, representing a nanostructured surface with a high local curvature (radius of curvature of ~10 nm). AFM imaging was performed after deposition of every three bilayers to probe the PEM growth on nanostructured surface (Fig. 2.2A-D). The images revealed no signs of aggregation or patchiness of PEM on AuNR after the deposition of multilayers. For a conformal PEM film, with the thickness of PEM on AuNR and adjacent planar regions being identical, the diameter of AuNR as measured from AFM images should remain constant. However, we observed that the PEM deposition resulted in a decrease in the apparent diameter, as measured from AFM height images of the nanorods, indicating a non-conformal PEM growth on the nanostructure surface (Fig. 2.2A-D). Cross-sections along the lines indicated in the AFM images clearly reveal a progressive decrease in the vertical dimension of AuNR with an increasing number of bilayers. The decrease in the vertical dimension of the nanostructures is due to the thinner deposition of PEM on nanostructures, as compared to that on the planar silicon surface surrounding the nanostructures. Although not explicitly stated, non-conformal growth of PEM was observed in previous spin-assisted LbL studies involving the deposition of multi-layers on inorganic nanostructures (e.g., AuNP, silver nanowires, QDs, CNTs). [41, 42, 43, 44] In the present method, the swelling of polymer films can be measured with no *a priori* knowledge of the thickness of the polymer film making the approach suggested here tolerant to local thickness variations.

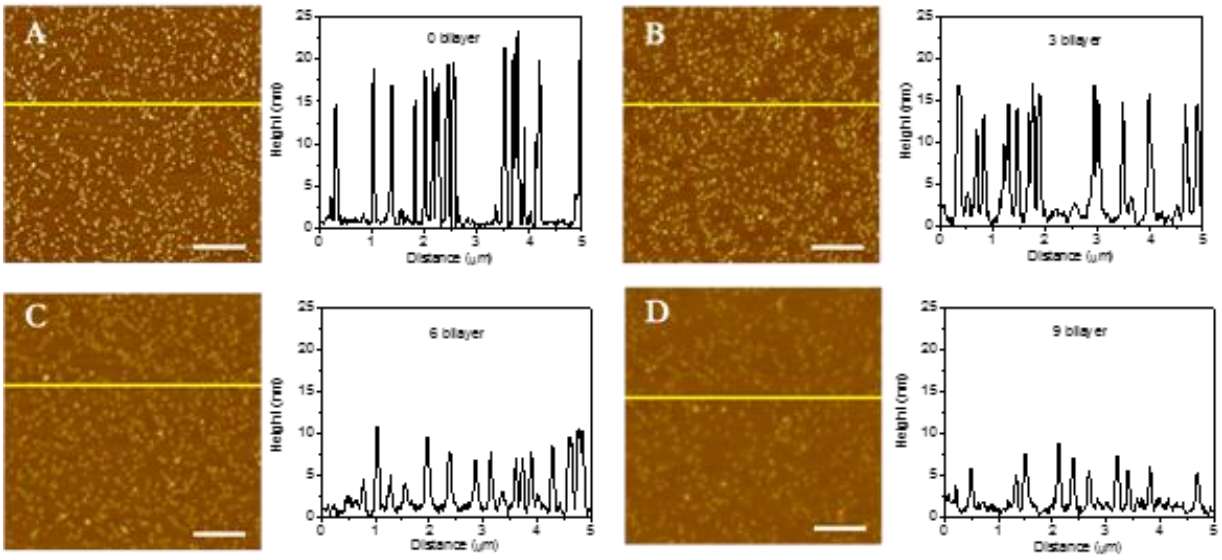

Figure 2.2 - AFM images of (A-D) AuNRs on P2VP covered by 0, 3, 6 and 9 polyelectrolyte bilayers respectively (scale bar is 1 μm, Z scale is 80nm), and corresponding cross-sectional height profiles.

2.3 Probing the Swelling of Ultra-Thin Films

For probing the swelling of the PEM, we employed longitudinal LSPR of AuNR due to the higher refractive index sensitivity, as compared to the transverse LSPR. [37] The refractive index sensitivity of the longitudinal plasmon band was found to be 146nm/RIU, which is obtained by changing refractive index of the surrounding medium (Fig. S.1). Extinction spectra collected following the deposition of each polyelectrolyte layer revealed a progressive red-shift in the LSPR wavelength and increase in LSPR intensity with the deposition of each layer due to the increase in the refractive index (from air to polymer layer) in proximity to nanorods (Fig. 2.3A). The longitudinal LSPR extinction band of AuNR deposited on surface exhibits a small shoulder due to the plasmon coupling between the nanorods. The extinction spectrum was deconvoluted by fitting the band with two Gaussian peaks, from which the LSPR wavelength and intensity were obtained (Fig. 2.3B). The peak corresponding to the plasmon resonance of the individual nanorods was employed to monitor the swelling of the PEM.

The incremental LSPR shift with the adsorption of each layer showed a progressive decay with the number of polyelectrolyte layers. This is a result of the decay in the refractive index sensitivity with increasing distance from the surface of the plasmonic nanostructures owing to the evanescent nature of the electromagnetic field at the surface of plasmonic nanostructures (Fig. 2.3C). The incremental shift of the LSPR wavelength provides a facile means to follow the adsorption of the polyelectrolytes on AuNR surface. The PEM were deposited on positively charged AuNR (due to capping with cetyltrimethylammonium bromide), starting with negatively charged PSS layer. Due to insufficient binding of the first PSS layer, the corresponding shift is relatively small compared to the following PAH layer. The incremental shift is expected to monotonically decrease with the increase of distance from AuNR surface if each adsorbed layer has the same thickness. However, we observed a saw-tooth pattern with higher incremental shift for PSS layer compared to the PAH layer of the same bilayer. Considering the negligible difference in the refractive index of PAH and PSS, [30ref] the higher shift of the PSS layer can be attributed to the higher amount of PSS adsorbed in each layer compared to PAH. The higher shift upon PSS layer adsorption is in agreement with the previous reports involving quartz crystal microbalance measurements, which demonstrate higher shift in resonance frequency for the PSS layer compared to the PAH layer. [38]

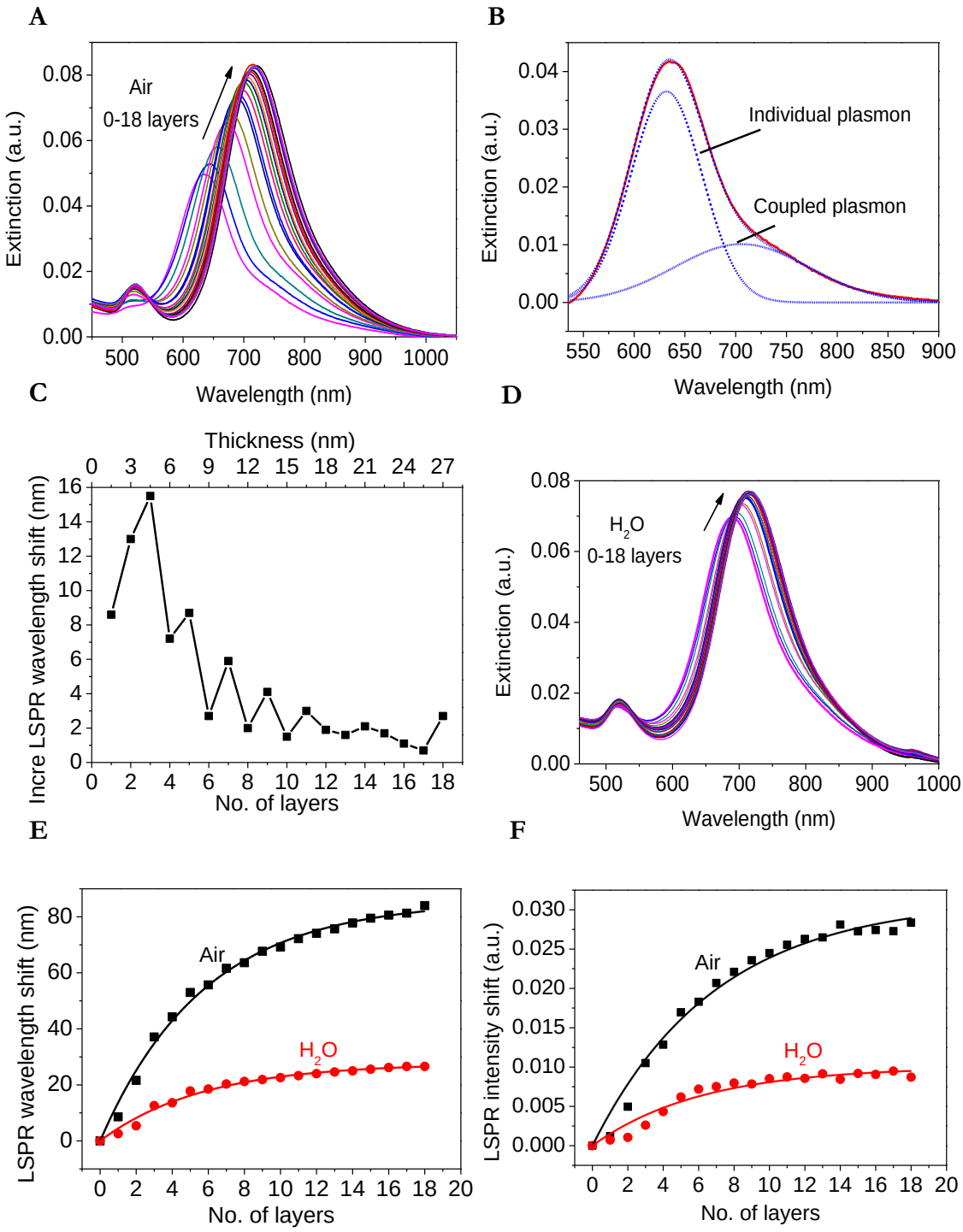

Figure 2.3 - Extinction spectra of AuNRs collected in (A) air and (D) H_2O after the deposition of each polyelectrolyte layer. (B) Representative extinction spectra of AuNR with peak deconvolution using two Gaussian peaks. (C) Incremental shift in air. (E,F) Cumulative LSPR wavelength and intensity shift of the longitudinal surface plasmon band of the AuNR with the number of bilayers.

Extinction spectra were also obtained in water following the deposition of each layer (Fig. 2.3D). The LSPR wavelength and intensity shift in water was found to be significantly smaller compared to that observed in air due to the fact that the change in refractive index with deposition of the bilayers is much smaller in water (water to polymer layer) compared to that in air (air to polymer) (Fig. 2.3E,F). Also, the swelling of the polyelectrolyte bilayers in water results in lowering the effective refractive index experienced by the nanorods. Owing to the evanescent nature of the electromagnetic field at the surface of the plasmonic nanostructures, the LSPR wavelength shift in air and water exhibit a characteristic decay with the increasing number of layers (*i.e.* distance from the surface of the nanorods), given by equation (1) [26, 45]:

$$R = m\Delta\eta\left(1-\exp\left(-d/l\right)\right)$$

where R is LSPR shift, m is the refractive index sensitivity of AuNR, $\Delta\eta$ is the change in the refractive index in RIU, d is the adsorbate layer thickness (thickness of the PEM in this case) and l is the plasmon decay length. The refractive index sensitivity (m) and plasmon decay length (l) of AuNR were calculated by fitting the experimental data of the LSPR shift in air using equation (1). Assuming the refractive index of the polyelectrolyte multilayer to be 1.56, [29ref] the refractive index sensitivity of the AuNR was found to be 153 nm/RIU, which closely agrees with independent measurements using various solvent mixtures (Fig. S.1). The plasmon decay length was found to be 5 nm, which corresponds to the distance from the surface of the nanorods at which the electromagnetic field intensity decreases by ~63%. [29]

To estimate the swelling of the PEM in water, the LSPR shift measured in water was fitted with equation (1). Although the thickness of the swollen bilayers is unknown, the fitting yields the pre-factor ($m\times\Delta\eta$) to the exponential term. From the known refractive index sensitivity of the nanorods (m=153 nm/RIU), obtained from the air measurements, the $\Delta\eta$ value in water was estimated to be 0.18 RIU. The obtained $\Delta\eta$ corresponds to the refractive index difference between swollen polymer layer and water (RI=1.33). Hence, the refractive index of swollen polymer layer was calculated to be 1.51 with LSPR wavelength and intensity shift.

The Maxwell-Garnett (MG) and Bruggeman (BG) equations were employed to calculate the thickness of the swollen polymer layer ($d_{swollen}$) from the refractive index of the swollen polymer layer. Those

equations relate the refractive index of the swollen polymer to the degree of swelling provided the refractive indices of the dry polymer layer (1.56) and solvent (1.33) are known. The Maxwell-Garnett and Bruggeman equations are given by equations (2) and (3), respectively [30, 46, 47, 48]:

$$n_F = n_M \sqrt{1 + \frac{3\phi}{\left(\frac{n_0^2 + 2n_M^2}{n_0^2 - n_M^2}\right) - \phi}}$$

$$\phi\left(\frac{n_0^2 - n_F^2}{n_0^2 + 2n_F^2}\right) + (1-\phi)\left(\frac{n_M^2 - n_F^2}{n_M^2 + 2n_F^2}\right) = 0$$

where n_F, n_0 and n_M are the refractive indices of the swollen polymer layer, dry polymer layer and the solvent respectively, and Φ is the volume fraction of the polymer layer within the swollen polymer layer, which is related to the layer thickness $d_{swollen}$ by $\phi = d_0 / d_{swollen}$, where d_0 is the thickness of dry film and $d_{swollen}$ is the thickness of swollen polymer layer. The percent swelling was calculated to be 26%, and 28% using (2) and (3), respectively, which is in close agreement with previously reported values for similar PEM systems. [31] The swelling of the polyelectrolyte layers was measured using nanorods with different aspect ratios (Fig. S.2). The swelling was found to be consistent within ±6%.

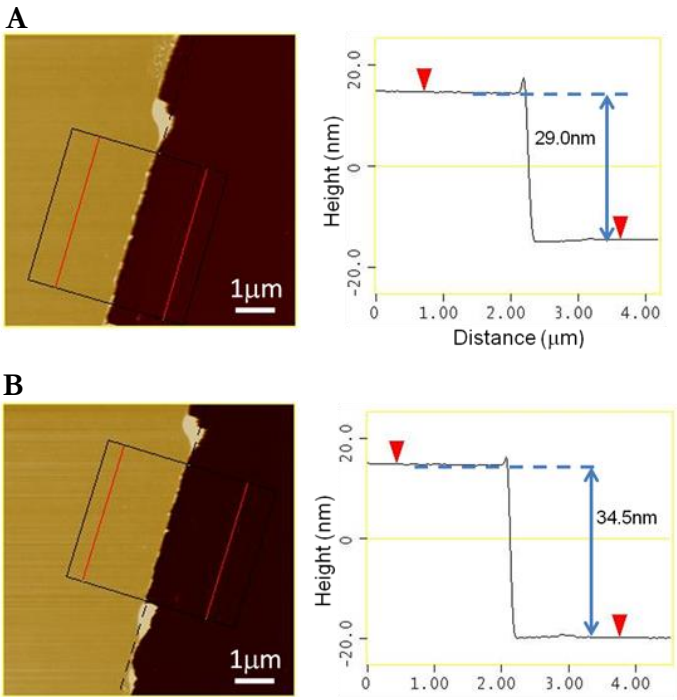

Figure 2.4 - AFM images along the edge of an intentional scratch in PEM film comprised of 9 bilayers collected in (A) air and (B) H_2O. Cross-sectional profile shows the difference in the thickness of the PEM film in dry and swollen state.

To confirm the swelling of the polyelectrolyte layers, AFM imaging was perfromed along the edge of an intentional scratch in PEM film comprised of 9 bilayers in air and H_2O (Fig. 2.4). Cross-sectional profiles have shown the difference in the thickness of the PEM film on the silicon surface in dry and swollen state. The swelling of the polyelectrolyte layers was measured to be 19%, which is extremely close to the value 26%±6% estimated using the gold nanorods (AuNRs) as plasmonic transducers.

2.4 Conclusion

In conclusion, we have demonstrated that plasmonic nanotransducers can be used to monitor the growth and swelling behavior of ultrathin polymer films with high resolution (down to single layer). Swelling of the polymer film can be measured with no *a priori* knowledge of the thickness of the polymer film, provided the refractive index of the polymer is known. The ability to quantitatively follow the small changes in refractive index with inexpensive UV-vis extinction spectrometer will form a powerful tool for monitoring the phase transition in ultrathin polymer films. The technique can be employed to study a variety of phase transitions in ultrathin polymers (such as glass transition, melting, crystallization), which involve perceivable changes in the refractive index of the polymer layer. Furthermore, highly localized refractive index changes, down to a single plasmonic nanostructure, can be achieved using dark-field scattering measurements.

Chapter 3

Novel SERS Probes with Built-In, Accessible EM Hotspots

3.1 Introduction

SERS is considered a powerful bioimaging modality for image-guided interventions in intraoperative settings. [49, 50, 51] Conventional contrast agents, often termed SERS probes, are comprised of individual, lightly aggregated, or assembled plasmonic nanostructures. These probes typically suffer from poor brightness, complex synthesis, or lack of stability in complex biological milieu. Nanoscale gaps between assembled or mildly aggregated plasmonic nanostructures are termed EM hotspots; such gaps host intense EM fields that enable single molecule SERS. [52] It has been demonstrated that the contribution of a relatively small number of EM hotspots (63 out of 106 active sites) can be quite significant (~25%) to the overall SERS signal, underscoring the importance of EM hotspots in the design of SERS probes. [53] To date, very few reported SERS probes based on individual nanostructures host built-in EM hotspots. [54, 55, 56] Of those reported probes, it has been shown that trapping Raman reporters in a sub-nm gap between a plasmonic core and shell greatly enhanced Raman signals from the reporter molecules. [54, 55] However, the EM hotspots in such core-shell nanostructures are not accessible to the surrounding biological environment, thus restricting these probes to simple structure contrast agents. Plasmonic nanoconstructs with built-in, yet accessible EM hotspots are ideal for SERS-based functional bioimaging i.e., imaging a specific (bio)chemical stimulus or molecular process. Here, we demonstrate a novel core-satellite nanoconstruct comprised of a shape-controlled plasmonic core and densely-packed satellites with sub-3 nm interstices that provide significantly stronger Raman signals than conventional designs. The large SERS enhancement combined with the accessible EM hotspots make the core-satellite nanoconstructs ideal for functional molecular bioimaging. Combined with tunable photothermal efficiency, these novel Au superstructures can serve as multifunctional theranostic agents.

3.2 Synthesis

Au nanoparticles on rod (AuNPRs), which are anisotropic plasmonic superstructures, are synthesized by coating AuNR cores with poly-L-histidine (poly-his), a biopolymer that enables the uniform nucleation of Au nanoparticles (satellites) on the AuNR core (Fig. 3.1). Due to the strong affinity of the histidine's imidazole group to Au ions, histidine-rich peptides have been employed to trap Au ions for the nucleation of Au nanocrystals on organic templates and for growing Au shells on quantum dots. [57, 58] Realization of AuNPR starts with the seed-mediated synthesis of AuNRs with a diameter of ~15 nm and a length of ~65 nm (Fig. 3.2B). Subsequently, the AuNRs are modified with a strong polyanion, specifically, PSS. The polyanion layer renders excellent stability to AuNR in a wide range of pH and ionic strength conditions, which is critical for the subsequent biopolymer adsorption and Au nanoparticle formation. Following the removal of excess PSS from the AuNR solution, poly-his is adsorbed on AuNR through its strong affinity to Au and electrostatic interaction with negatively charged PSS. The presence of PSS and poly-his on the AuNR was confirmed by zeta-potential measurement and SERS (supplementary Fig. S.3). For growing the Au satellites on AuNR, chloroauric acid ($HAuCl_4$), which serves as Au precursor, is introduced into the poly-his modified AuNR. Adsorption of poly-his on AuNR and subsequent capture of Au^{3+} ions by poly-his resulted in a red shift of 8.5 nm and 16.0 nm in the transverse and longitudinal LSPR wavelength of AuNR, respectively (Fig. 3.2A). Subsequently, polyvinylpyrrolidone (as a capping agent) and ascorbic acid (as a mild reducing agent) are introduced into the reaction solution to yield the formation of satellite clusters on AuNR surface (Fig. 3.2C).

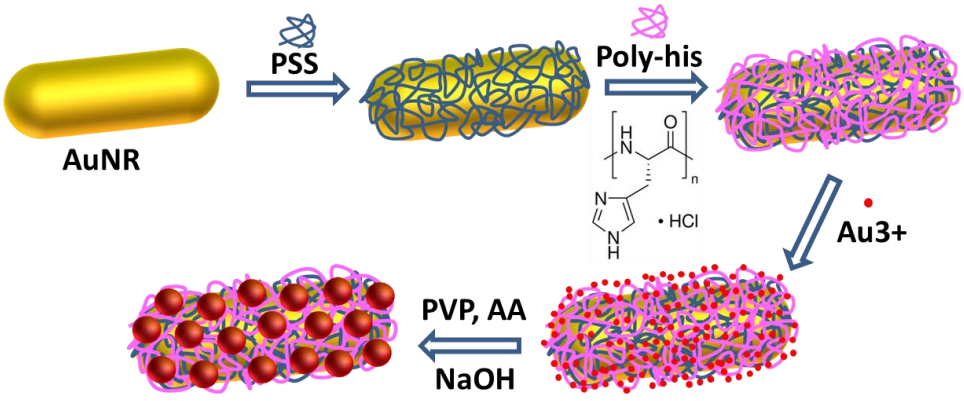

Figure 3.1 - Schematic illustration depicting the synthesis of Au nanoparticle on nanorod (AuNPR) superstructures by modifying the AuNR with a biopolymer, poly-L-histidine (poly-his), and subsequent growth of Au nanoparticles on AuNR surface.

Plasmon coupling between the core and satellite cluster and the increased dimension of AuNR resulted in a red shift of 40.5 nm in the transverse and 111.0 nm in the longitudinal LSPR wavelength (Fig. 3.2A). The strong affinity of poly-his to Au^0 and Au^{3+} ions facilitates the uniform nucleation and growth of Au nanocrystals on the AuNR core, as revealed by TEM images (Fig. 3.2B, 3.2C). In the

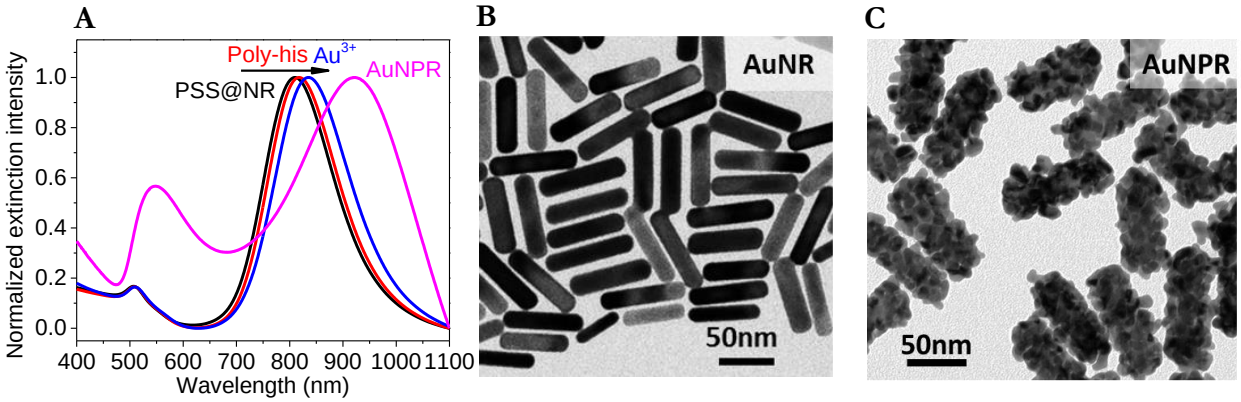

Figure 3.2 - (A) Normalized extinction spectra of AuNR, poly-his modified AuNR before and after binding Au^{3+} ions, and AuNPR showing the progressive red shift in LSPR wavelength due to increase in effective refractive index during surface modification and plasmon coupling after the growth of Au nanoparticles. Representative TEM images of (B) AuNRs and (C) AuNPRs.

absence of the poly-his coating, poor control over growth of Au nanoparticles on PSS-coated AuNR was noted, which suggests the importance of poly-his in the uniform growth of Au satellites on AuNR (supplementary Fig. S.4). The size and areal density of gold nanoparticles grown on AuNR core, which determine the optical properties of the superstructures, can be tuned over a broad range by varying the amount of Au precursor in the growth solution (supplementary Fig. S.5). The pH of the reaction solution also played an important role in the uniform nucleation of Au satellites on AuNR cores, with the optimal pH being 6.4 (supplementary Fig. S.6). A similar synthesis strategy can be employed for other shape-controlled nanostructures, such as on Au nanospheres (AuNS), which resulted in Au nanoparticles on spheres (AuNPS) (Fig 3.3B, 3.3C). Following the growth of Au satellites, the LSPR wavelength of AuNS exhibited a red shift of 50.0 nm, corresponding to the plasmon coupling between the core and satellites and the increase in diameter (Fig 3.2A). The novel biotemplated synthesis approach demonstrated here serves as a universal method to realize size- and shape-controlled plasmonic superstructures.

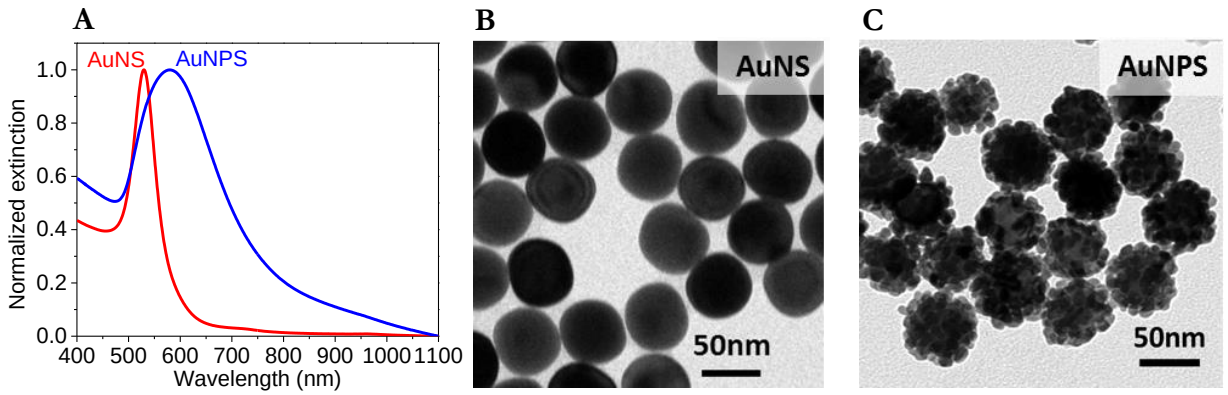

Figure 3.3 - (A) Normalized extinction spectra of AuNS and AuNPS showing the red shift in LSPR wavelength due to the plasmon coupling between the Au nanoparticles and the core. Representative TEM images of (B) AuNS, and (C) AuNPS showing the uniform growth of Au nanoparticles on the cores.

3.3 SERS Performance

Electromagnetic hotspots formed by controlled aggregation or assembly of plasmonic nanostructures are known to be highly SERS-active. [59, 60, 61] However, the poor stability in biological milieu of aggregates or assemblies of plasmonic nanostructures, formed through weak interactions such as electrostatic or hydrogen bonding, imposes severe challenges in achieving quantitative SERS-based bioimaging. The plasmonic superstructures with built-in EM hotspots demonstrated here can overcome the aforementioned challenges. High-resolution transmission electron microscopy (HRTEM) images of AuNPR and AuNPS reveal sub-3 nm interstices formed between the satellites on AuNR and AuNS surface (Fig. 3.4A, 3.4B). These interstices are open and accessible to

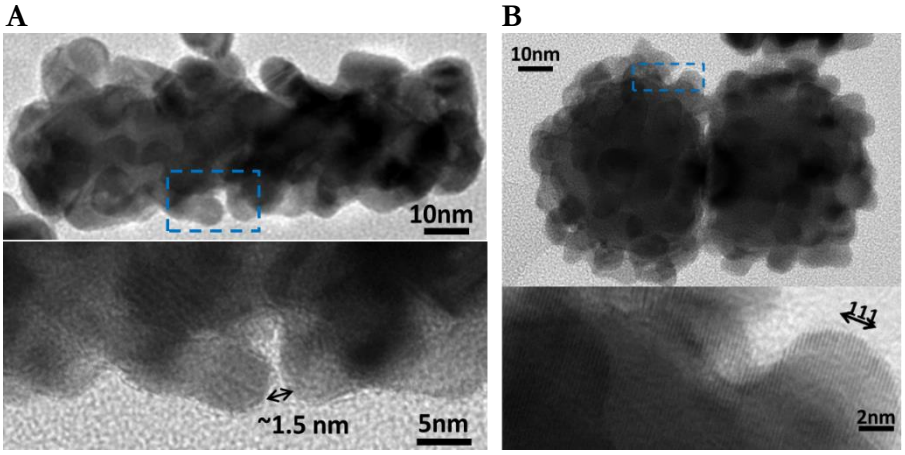

Figure 3.4 - High-resolution TEM (HRTEM) images showing the sub-3 nm interstices between the satellites in (A) AuNPR and (B) AuNPS, which serve as built-in electromagnetic hotspots and provide high SERS activity.

surrounding solvent environment, enabling diffusion of Raman reporter molecules into the EM hotspots and, more importantly, facile sampling of the surrounding environment. Following the adsorption of Raman reporter, p-mercaptobenzoic acid (pMBA), SERS spectra collected from the superstructure solutions revealed strong SERS signals corresponding to the reporter molecules (Fig. 3.5A, 3.5B and supplementary Fig. S.8A). As noted earlier, the size and areal density of the satellites on the AuNR core, which determine the density, intensity and accessibility of the EM hotspots, were found to significantly influence the SERS activity of the superstructures (supplementary Fig. S.8B, S.8C). Compared to the corresponding cores, AuNPR and AuNPS exhibited approximately 20 and 200 times higher SERS intensity, respectively (Fig. 3.5A, 3.5B). Finite-difference time-domain (FDTD) simulations confirmed the large enhancement of EM field in the interstices between the satellites (Insets of Fig. 3.5A, 3.5B). Nanostructures with such highly developed morphology and built-in EM hotpots preclude the need for controlled aggregation or assembly of plasmonic nanostructures to achieve high SERS activity. Interestingly, despite the weak plasmonic extinction in the NIR region, AuNPS exhibited very strong SERS signals with 785 nm excitation due to the EM hotspots formed between the satellites. This observation is in agreement with the recent demonstration that in a hotspot dominated nanoparticulate system, plasmonic assemblies of different geometries and LSPR wavelengths invariably exhibited high SERS enhancement under NIR excitation. [59]

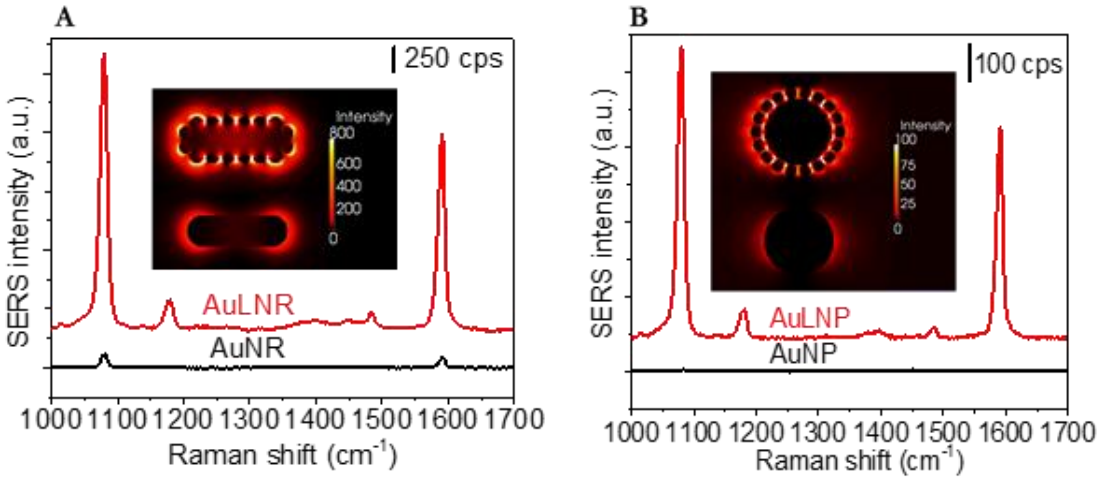

Figure 3.5 - Average SERS spectra obtained from (A) AuNR and AuNPR and (B) AuNS and AuNPS solution following the adsorption of Raman reporters (p-mercaptobenzoic acid) on the surface of the nanostructures. The SERS spectra demonstrate significantly higher SERS activity of the superstructure compared to the cores, owing to the EM hotspots associated with the superstructures. Finite difference time domain (FDTD) simulations, shown as insets of (A) and (B), confirm the EM hotspots of the plasmonic superstructures.

Chapter 4
Au Superstructures as Multifunctional Probes

4.1 Introduction

To the best of our knowledge, individual plasmonic nanostructures as SERS probes have not been employed for spatiotemporal mapping of living cells to quantify intravesicular pH changes along endocytic pathways and exocytosis of internalized nanomaterials. Currently, pH in living cells is primarily quantified using fluorescent dyes that are plagued by photobleaching, low fluorescence quantum yield and narrow pH probing range. [62, 63, 64] SERS, on the other hand, is highly attractive for functional molecular bioimaging owing to numerous advantages including high sensitivity and specificity, excellent photostability, absence of interference from water, and high spatial resolution.[1-3] However, most pH-sensitive SERS probes rely on the assemblies or aggregates of gold or silver nanoparticles to improve the brightness. [65, 66, 67] For demonstrating the intracellular pH imaging ability of AuNPRs, we have employed human renal adenocarcinoma cell line 786-O as a model cell line. To ensure the serum stability and biocompatibility of Au superstructures, we coated the superstructure surface with thiol-modified polyethylene glycol (SH-PEG), a non-toxic and hydrophilic polymer as a protective layer. [50, 68] The stability of AuNPRs were confirmed by monitoring the vis-NIR extinction spectra of PEGylated AuNPRs-pMBA at several time points following their dispersion in 10% fetal bovine serum (FBS) at 37 °C. The extinction spectra of AuNPRs-pMBA shows ~2 nm of red shift in the longitudinal LSPR wavelength within the first 6 hours, corresponding to non-specific adsorption of serum proteins (supplementary Fig. S.5A). The biocompatibility of AuNPRs-pMBA was verified by performing (3-(4,5-dimethylthiazol-2-yl)-2,5-diphenyltetrazolium bromide (MTT) cell viability assay (supplementary Fig. S.7B, S.7D). The concentration of superstructures at which the cell viability was at least 85% or higher (compared to the control cells) was chosen for subsequent studies.

4.2 AuNPRs as pH Probes

To demonstrate the functional molecular bioimaging capability of superstructures by utilizing the accessible EM hotspots, we employed pMBA as a pH sensitive Raman reporter to monitor the pH of the aqueous surroundings. After confirming high SERS activity of superstructures as discussed in §2.3, we collected SERS spectra from pMBA-modified AuNPRs dispersed in different pH buffers ranging from pH 5 to pH 9 with a 0.5 pH unit interval (Fig. 4.1A, S.8D). The SERS spectra from

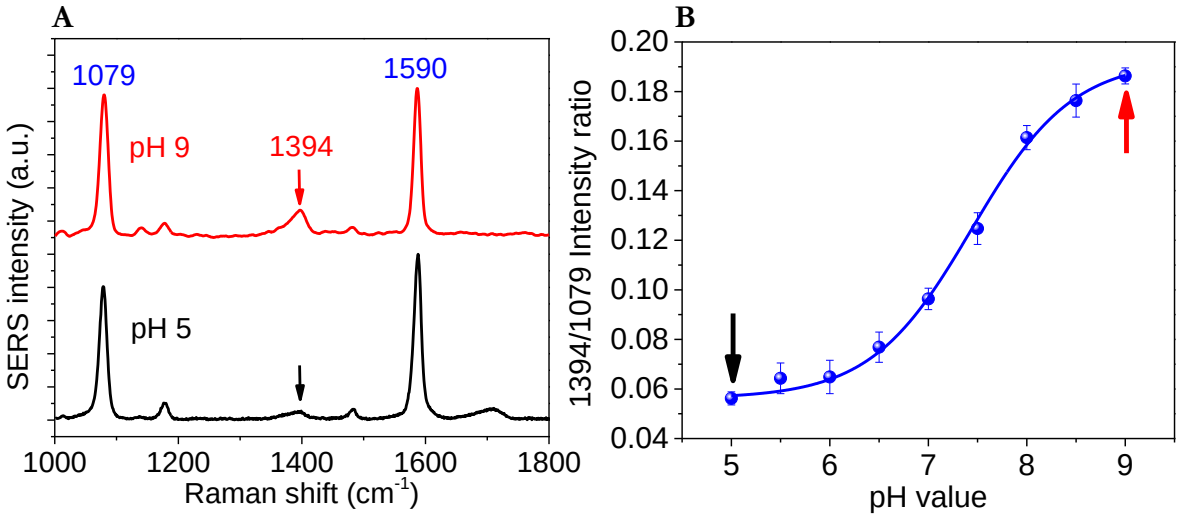

Figure 4.1 - (A) Representative SERS spectra from AuNPR at pH 5 and 9, showing the increase in the ratio of relative Raman intensity of symmetric carboxylate stretching band of pMBA at 1394 cm-1 to 1079 cm-1 with increasing pH due to the deprotonation of the carboxylate group. (B) A pH calibration plot showing the variation of the ratio of intensity of Raman bands at 1394 and 1079 cm-1 with external pH.

AuNPR show two strong Raman bands at 1079 cm^{-1} and 1590 cm^{-1}, corresponding to the aromatic ring mode of pMBA. The ratio of the intensities of symmetric carboxylate stretching band (at 1394 cm^{-1}) and aromatic ring mode of pMBA (at 1079 cm^{-1} or 1590 cm^{-1}) was found to increase with pH due to the deprotonation of the carboxylate group. [65] The measured pKa value of pMBA adsorbed on AuNPR surface is around 7.4, which is close to physiological pH and makes it an ideal Raman reporter for probing pH in biological applications. [65] A pH calibration curve was obtained by plotting the intensity ratio of Raman bands 1394 cm^{-1} / 1079 cm^{-1} as a function of pH (Fig. 4.1B). Since the pH is correlated to the ratio of the intensity of the two bands, the absolute intensity of the Raman bands, determined by the number of AuNPR in the focal volume, is not very important, given that the intensity of the two Raman bands is sufficiently high.

4.3 Spatiotemporal pH Mapping of Living Cells

We incubated 786-O cells seeded on a quartz substrate with PEGylated AuNPRs-pMBA to facilitate internalization, followed by the removal of free AuNPRs. The uptake of AuNPRs by 786-O cells is facilitated by micropinocytosis and receptor-mediated endocytosis due to non-specific adsorption of serum proteins on AuNPR surface (Fig. 4.2, 4.3A). [69, 70] After internalization, AuNPRs

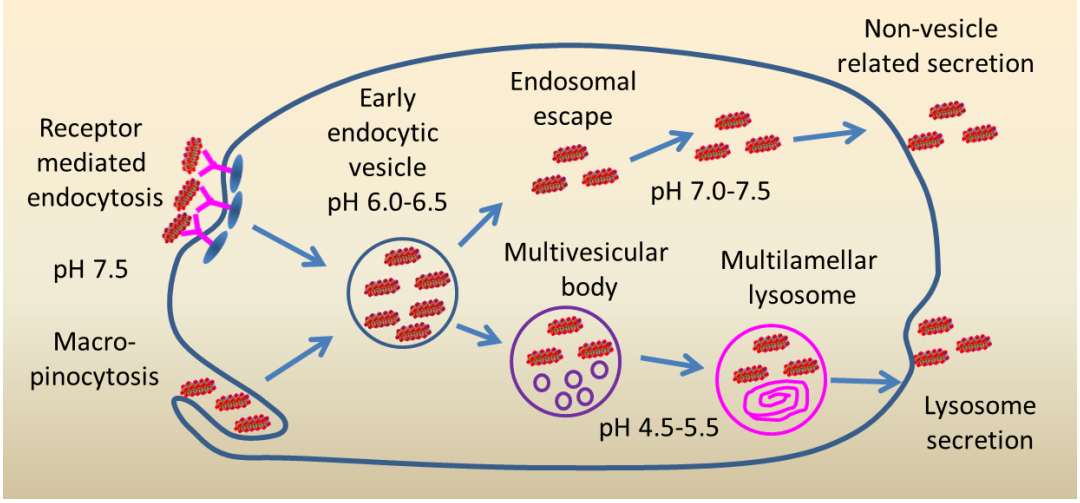

Figure 4.2 - Schematic depicting the endocytosis, intracellular transportation, and exocytosis of AuNPRs.

encapsulated inside intracellular compartments go through an endocytic pathway with a characteristic acidification profile from pH 6.0-6.5 in early endocytic vesicles to pH 4.5-5.5 in multivesicular bodies (MVBs) and multilamellar lysosomes (MLs). Some of the internalized AuNPRs escape from endosomes to cytosol (pH 7.0-7.5) and directly exocytose from cells (Fig. 4.2). [71] TEM images of ~100 nm thick cell sections reveal uptake of AuNPRs by micropinocytosis and AuNPRs-trafficking vesicles in a size range of 0.5-2.0 μm, including small early endocytic vesicles, large MVBs containing many small luminal vesicles, and MLs with characteristic membrane whorls enclosed (Fig. 4.3A-D). It is important to note that the internalized AuNPRs preserve the core-satellite superstructure, which is critical for their high SERS activity (Fig. 4.3B).

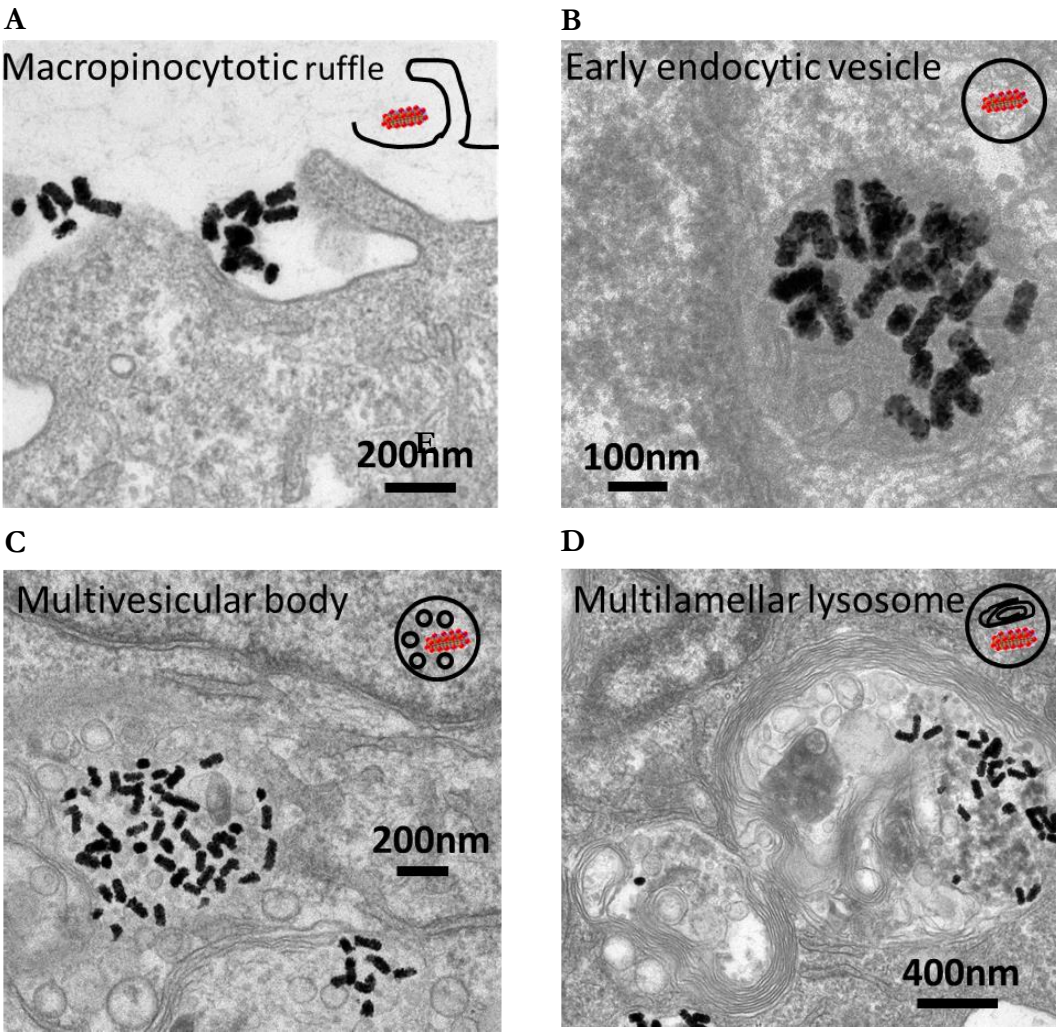

Figure 4.3 - AuNPRs enter the cell by receptor-mediated endocytosis and non-specific micropinocytosis, evidenced by TEM image (A). After internalization of AuNPRs, the intravesicular pH drops along the endocytic pathway, from pH 6.0-6.5 in early endocytic vesicles (B) to pH 4.5-5.5 in multivesicular bodies and multilamellar lysosomes (C, D). The AuNPR preserve their highly developed core-satellite structure even after internalizing into the cells, which is critical for their high SERS activity.

Raman imaging was performed using a live cell chamber under a confocal Raman microscope after locating the cells under dark-field illumination. The intensity maps of Raman band at 1079 cm^{-1} obtained at 0, 30 and 60 min using a 785 nm laser as excitation source enabled the clear delineation of the cells shape (Fig. 4.4A1, 4.4B1, 4.4C1). Dark-field optical images of the cells revealed the large Rayleigh scattering from the internalized and cell surface-bound AuNPRs (inset images of Fig. 4.4A2-4.4C2). Raman intensity histograms obtained from intensity maps at different time points showed

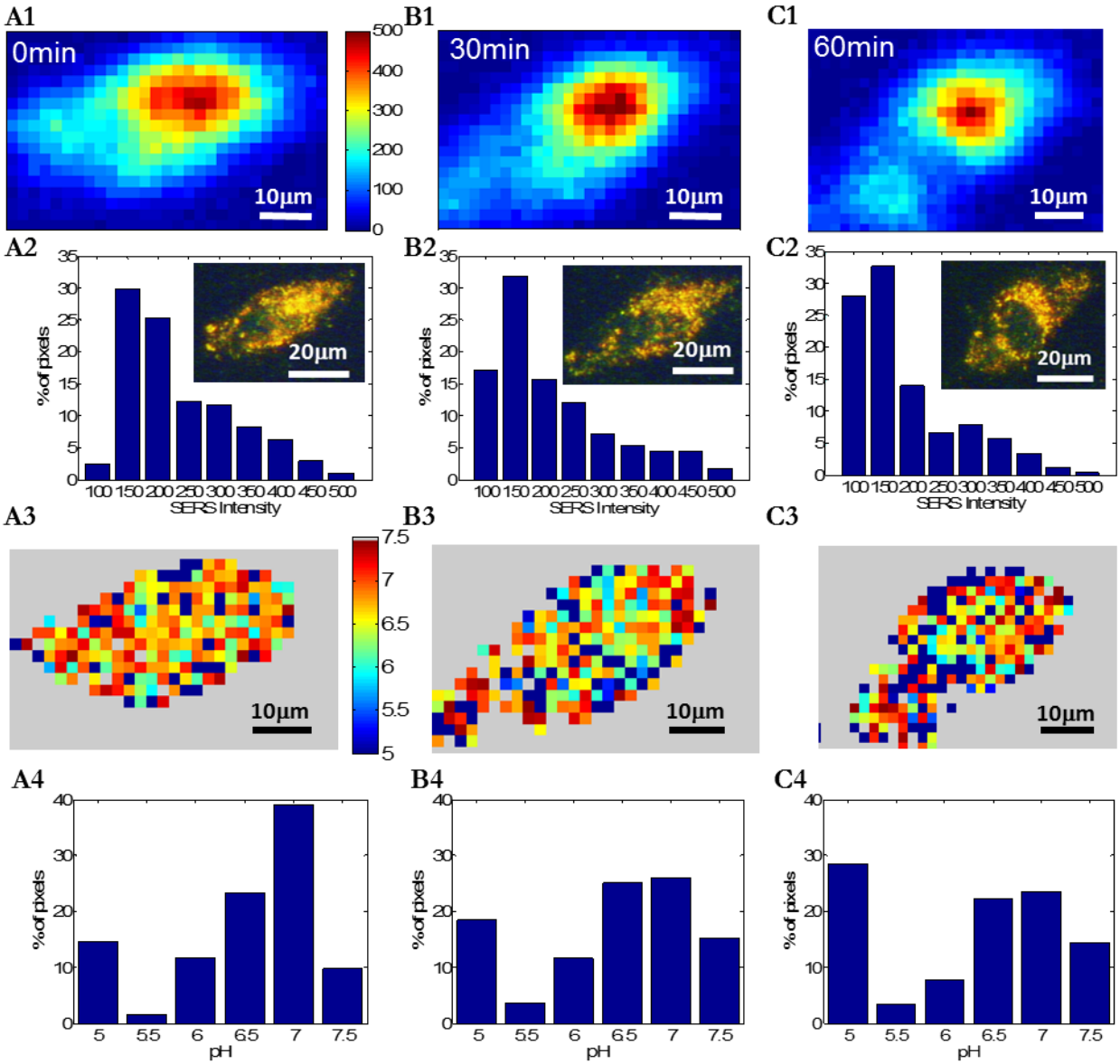

Figure 4.4 - Spatiotemporal mapping of SERS intensity and pH changes using AuNPRs in a living 786-O cell. (A1, B1, C1) SERS intensity map of 1079 cm^{-1} Raman band of pMBA at different time points, showing the clear delineation of the shape of the cell spread on a quartz substrate and (A2, B2, C2) corresponding histograms analyzed from intensity maps with ~10% mean intensity drop after every 30 min. Dark field optical microscope was used to locate the cell and match the cell margin with intensity maps (Insets of A2, B2, C2). (A3, B3, C3) Spatiotemporal pH maps analyzed from the intensity ratio of Raman bands 1394 cm^{-1} /1079 cm^{-1} based on the built pH calibration curve at each pixel color-coded using MATLAB®. (A4, B4, C4) The time-dependent pH histograms show the decrease in the number of pixels corresponding to physiological pH 7.0-7.5 from 49% to 38% and increase in the number of pixels corresponding to acid pH 4.5-5.5 from 16% to 32%, which visualize the intravesicular pH drops in the endosomal maturation process.

~10% mean intensity drop after 30 min duration and ~20% drop after 60 min (Fig. 4.4A2, 4.4B2, 3.4C2). The intensity drop corresponds to the ~20% exocytosis of AuNPRs within 1 h. We validated the exocytosis fraction using a conventional method to quantify the change of gold content after exocytosis by inductively coupled plasma mass spectroscopy (ICP-MS). ICP-MS measurements indicated an average uptake of nearly 7.1×10^3 AuNPRs per cell after 8 h of incubation, which is slightly higher than reported values probably due to the differences in size, shape, surface coating, initial concentration, incubation time and sedimentation effect of nanoparticles and cell lines. [69, 72] ICP-MS results also showed ~20% decrease in gold content of cells over 1 h of incubation in complete medium at 37°C, confirming the exocytosis fraction calculated from Raman intensity maps, which is also in agreement with typical exocytosis fraction reported previously. [73]

Intracellular pH maps were obtained by comparing the intensity ratio of Raman bands at 1394 cm^{-1} and 1079 cm^{-1} at each pixel with a pH calibration curve shown in Fig. 4.1B. Each pixel was color-coded using MATLAB®, with red to blue representing the progressive transition from physiological pH to more acidic values (Fig. 4.4A3, 4.4B3, 4.4C3). The physiological pH 7.0-7.5 corresponds to AuNPRs on the cell surface or at a very early stage of internalization in close proximity to the cell membrane, or those that escaped from endosomes. The time-dependent pH histograms showed the decrease in the fraction of physiological pH 7.0-7.5 from 49% to 38% after 1 h, suggesting that some surface bound AuNPRs proceed to early endosomes and the AuNPRs that escaped from endosomes are exocytosed (Fig. 4.4A4, 4.4B4, 4.4C4). The fraction of pH 6.0-6.5 decreased from 35% to 30%, indicating the trafficking of AuNPRs from early endosomes to more acidic MVBs and MLs. The trafficking is also confirmed by the increase in the fraction of pH 5.0-5.5 from 16% to 32% by 1 h, which visualizes the intravesicular pH drops in the endosomal maturation process. The overall dynamics of pH values in a living cell along the endosome maturation pathway agrees with previous reports. [67, 74] Owing to the accessible electromagnetic hotspots that enable facile sampling of the surrounding environment, Au superstructures are excellent candidates for functional molecular bioimaging. Previous SERS probes with built-in hotspots rely on layered architecture with Raman reporters trapped between the core and shell, which precludes their exposure surrounding environment and limits them to simple structure contrast agents. [54, 55]

4.4 AuNPRs for Locoregional Therapy

Next, we turn our attention to photothermal efficacy of the Au superstructures comprised of AuNR and AuNS cores. The temperature rise of AuNPR and AuNPS solutions upon irradiation with 808 nm laser (at a power density of 0.3 W/cm^2) was monitored using an infrared camera (Fig. 4.5A, 4.5B). The temperature of the superstructure solutions exhibited significant increase within the first 100 S of irradiation followed by either small increase or stabilization for subsequent irradiation. At t = 300 S, AuNPR exhibited nearly 24°C rise in temperature while AuNPS exhibited significantly smaller rise in temperature (~8°C) under identical conditions. The significantly higher rise in temperature of AuNPR solution compared to AuNPS solution can be rationalized from the vis-NIR extinction spectra of these nanostructures, which demonstrate the significantly higher absorbance of the AuNPR at 808 nm compared to AuNPS at the similar concentration of ~55 μg/ml Au atoms.

To test the photothermal therapeutic ability of the Au superstructures *in vitro*, 786-O cells at 90% confluence in 24 well plates were incubated with AuNPR and AuNPS to facilitate internalization of the nanostructures. Following the removal of free Au superstructures, the cells were irradiated with 808 nm laser for different durations (0-6 min) followed by incubation at 37°C and 5% CO_2 for 18 hrs. Cell viability quantified by MTT assay indicated significantly higher cell death for different irradiation times for AuNPR compared to that of AuNPS, which is in complete agreement with the higher photothermal efficiency of AuNPR compared to AuNPS (Fig. 4.5C). Whereas the viability of cells incubated with AuNPS remains at 80% even after irradiation for 6 min, the viability of cells incubated with AuNPR drops to 10% for the same irradiation conditions. These results were further confirmed by a live/dead cell assay performed after 6 min of irradiation for cells incubated with AuNPS and AuNPR (Fig. 4.5D). Presence of strong green fluorescence (corresponding to the live cells) and absence of red fluorescence (corresponding to the dead cells) was noted for cells incubated with AuNPS following laser irradiation, whereas the inverse was noted for cells incubated with AuNPR. AuNPRs, which exhibit strong SERS activity and absorbance in the NIR wavelengths, serve as multifunctional theranostic probes that can be employed to image and treat cancer. On the other hand, AuNPS, which exhibit weak absorbance but strong SERS activity using near infrared excitation can efficiently decouple imaging from unwanted photothermal heating (Fig. 4.5B, supplementary S.11).

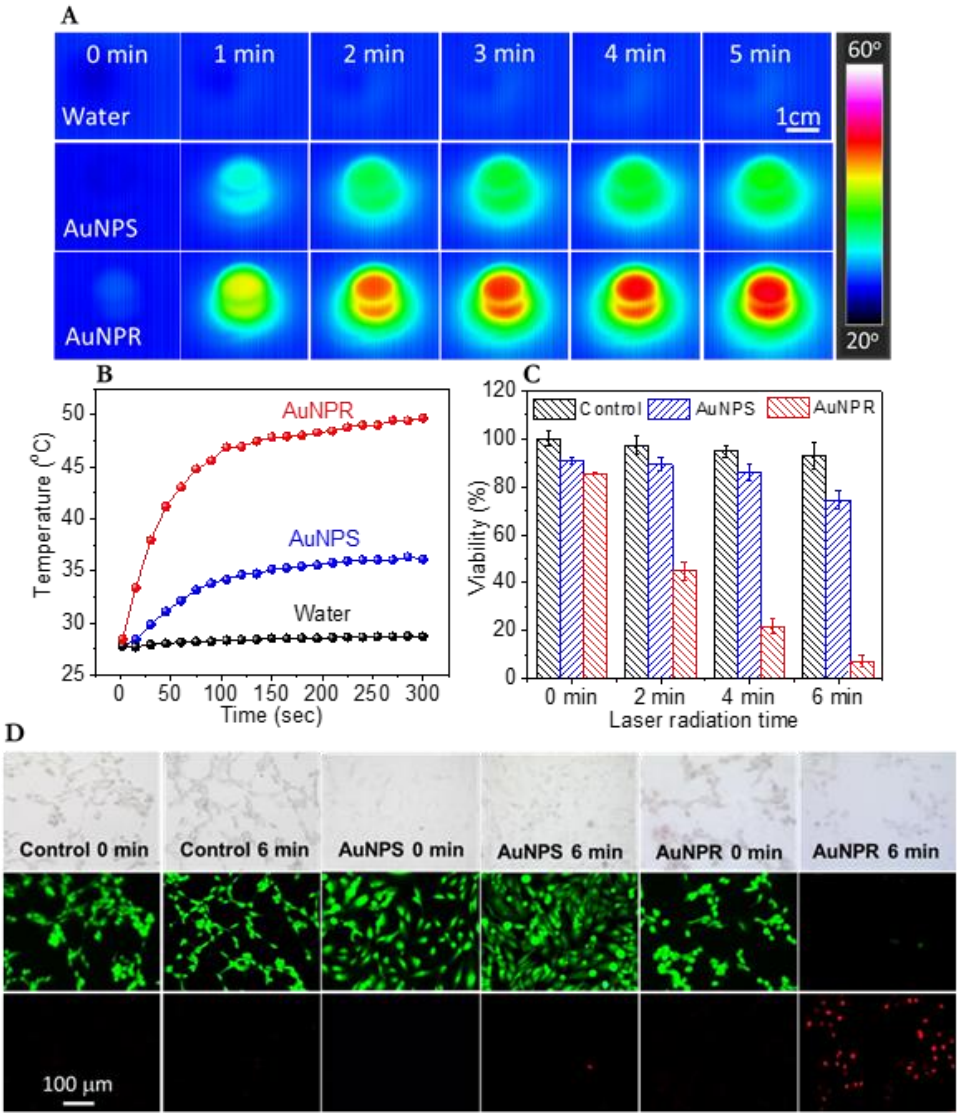

Figure 4.5 - Shape-dependent photothermal efficiency of Au superstructures. (A) Infrared images depicting the rise in the temperature of water, AuNPS and AuNPR upon irradiation with NIR laser (λ_{ex} = 808 nm) at a power density of 0.3 W/cm². (B) Plot showing the significantly higher rise in temperature of AuNPR solution (ΔT= 24° C) compared to AuNPS (ΔT= 8° C) and water (ΔT= <1° C) upon irradiation with NIR laser. (C) Cell viability following the NIR laser irradiation of control cells and cell incubated with AuNPS and AuNPR for different durations as quantified by MTT assay. While the control cells and cells incubated with AuNPS exhibit high viability consistent with the small rise in temperature, cells incubated with AuNPR exhibited significant reduction in viability. (D) Bright field (top row), green (middle row) and red (bottom row) fluorescence images of control cells and cells incubated with AuNPS and AuNPR. Following the irradiation with NIR laser (λ_{ex} = 808 nm), control cells and cells incubated with AuNPS exhibited green fluorescence (indicating live cells) while cells incubated with AuNPR exhibited red fluorescence (indicating to dead cells).

4.5 Conclusion

In conclusion, we have demonstrated a simple and universal approach to synthesize plasmonic superstructures comprised of a shape-controlled Au core and densely packed Au satellites. The biotemplated approach demonstrated here can be extended to any Au nanostructure to obtain superstructures with desired optical properties. As opposed to conventional structural SERS imaging probes, core-satellite superstructures with accessible electromagnetic hotspots can serve as functional contrast agents, able to sense and report a specific (bio)chemical stimulus or molecular process in complex biological milieu. Furthermore, in these EM hotspot-dominated superstructures, the SERS activity can be decoupled from LSPR wavelength, making them ideal for unperturbed bioimaging. Conversely, the superstructures can be designed to serve as imaging and therapeutic agents by rational choice of the size and shape of the Au cores.

Appendix A

Experimental Information

A.1 Characterization

TEM images were obtained using either field emission TEM (JEM-2100F, JEOL) or JEOL 2010 LaB6 operating at an accelerating voltage of 200 kV. Samples were prepared by drying a drop of the solution on a carbon-coated grid, which had been previously made hydrophilic by glow discharge. UV−vis extinction spectra were collected using a Shimadzu 1800 spectrophotometer. AFM micrographs were obtained using Dimension 3000 (Digital instruments) AFM in light tapping mode. [75] Triangular Si cantilevers with tip radius less than 10 nm (MikroMasch) were employed for AFM imaging. Zeta potential measurements were performed using Malvern Zetasizer (Nano ZS). Raman spectra were collected using a Renishaw inVia confocal Raman spectrometer mounted on a Leica microscope with 20X objective (NA = 0.40) in the range of 600−1800 cm^{-1} with one accumulation and 10 s exposure time. A 785 nm wavelength diode laser coupled to a holographic notch filter was used to excite the sample.

A.2 Adsorption of AuNR on Glass Surface

The glass substrate deposited with gold nanorods was fabricated by modifying the substrate with poly(2-vinyl pyridine) (P2VP) by exposing the piranha cleaned glass surface to 4% (w/v) P2VP solution in ethanol. After rinsing the substrate with ethanol, it was exposed to gold nanorod solution to enable adsorption of the gold nanorods. Finally, the substrate was rinsed with water to remove the loosely bound nanorods, leaving a highly dense layer of nanorods on the surface.

A.3 Calculating Refractive Index Sensitivity of AuNR

The glass substrate adsorbed with gold nanorods was measured in different solvents, which are are air, H2O, and 20%, 37%, 52% (w/v) sucrose solution. For each solvent, the extinction spectrum was collected with keeping a reference substrate in the same solvent environment. After deconvoluting

each spectrum with Gaussian fit, the LSPR wavelength of the second peak was used to calculate the refractive index sensitivity of AuNRs (Fig. S.1).

A.4 Polyelectrolyte LbL Assembly

The glass substrate adsorbed with gold nanorods was rinsed with water three times to remove CTAB on AuNRs surface before LbL deposition until stable extinction spectra were obtained. LbL assembly was performed using the PSS as polyanion and PAH as polycation. Glass substrates were spin coated (3000 rpm, 20 sec) with PAH and PSS alternately from 0.2% (w/v) polymer solutions in nanopure water. The sample was rinsed with water twice after each layer to remove excess polymer.

A.5 SERS Imaging of Live Human Cells

Human renal cancer cell line (786-O) was sub-cultured in RPMI-1640 medium with 10% fetal bovine serum (FBS) and antibiotics (100 μg/ml penicillin/streptomycin) while renal proximal tubule cells (RPTEC) were cultured in RPMI-1640 medium with 10% fetal bovine serum (FBS) and 100 μg/ml of G418 Sulfate. Cells were grown in a water jacket incubator at 37 °C with 5% CO_2-humidified atmosphere in 25 cm^2 tissue culture flasks. Once the cells reached 90% confluence, they were washed with phosphate buffered saline (PBS) and detached with 2 ml of 0.25% trypsin-EDTA solution. After centrifugation, cells were dispersed in complete medium with 10% FBS and plated at a density of 1×10^4 cells/ cm^2 on a quartz substrate in a 35 mm flat-bottom culture dish. After overnight incubation at 37 °C with 5% CO_2-humidified atmosphere, 786-O cells were incubated with 3 ml of PEGylated AuNPRs-MBA dispersed in complete medium for 8 hours at 37 °C. Then the cells were thoroughly rinsed with PBS twice to remove loosely bound AuNPRs on the cell surface and mounted on a live cell chamber with well controlled temperature and CO_2. After locating the cells using a dark-field microscope, the living cell imaging was performed using a confocal InVia Renishaw Raman microscope by collecting a 2D array of Raman spectra with 2 μm of spatial resolution using a 785 nm laser with 3 mW power using 20X objective and 3 sec exposure time. A live/dead cell assay was performed to ensure the viability of cells after the living cell imaging (supplementary Fig. S.9). Correspondingly, the cells were prepared the same way for TEM section imaging.

A.6 *In Vitro* Photothermal Therapy

The NIR irradiation was performed using an 808 nm wavelength diode laser for different durations at a power density of 400 mW cm^{-2}. Following laser treatment, the cells were incubated with full medium for 16 hours and then stained with ethidium homobromide-1 and calcein AM dyes to produce green and red emission from live and dead cells, respectively. Methylthiazolyldiphenyl-tetrazolium bromide (MTT) assay was employed to probe the viability of 786-O cells. 10 µl of MTT in PBS (5 mg/ml) was added to each well, followed by 4 hours of incubation. Subsequently, 100 µl of dimethyl sulfoxide (DMSO) was added to each well, including controls, followed by gentle swirl. The absorbance was measured at 570 nm using an Infinite F200 multimode reader (Tecan, Switzerland). Cell viability was normalized to that of 786-O cells cultured in the complete culture medium without the incubation with AuNPRs/AuNPSs-MBA.

A.7 Polyelectrolyte Coating of AuNR/AuNP

AuNRs/AuNPs were modified with polyelectrolytes as previously reported. [76] Briefly, 1 ml of twice centrifuged AuNRs solution was added drop-wise to 0.5 ml of PSS solution (0.2% w/v) in 6 mM NaCl aqueous solution under vigorous stirring, followed by shaking for 3 h. To remove excess PSS, the above solution was centrifuged at 10,000 rpm for 10 min, and the pellet was dispersed in nanopure water after removing the supernatant. The surface charge of CTAB stabilized AuNRs, PSS coated AuNRs (AuNRs@PSS) were estimated by measuring the zeta potential of corresponding solution (Fig. S.3).

A.8 Cell Viability Assay

To quantify the toxicity of nanomaterials, Methylthiazolyldiphenyl-tetrazolium bromide (MTT) assay was employed to probe the viability of 786-O cells incubated with various concentrations of PEGlated AuNPRs-MBA for 4 h. 10 µl of 5 mg/ml MTT in PBS was added to each well, followed by 4 hours of incubation. Then 100 µl of dimethyl sulfoxide (DMSO) was added to each well, including controls, followed by gentle swirl. The absorbance was measured at 570 nm using an Infinite F200 multimode reader (Tecan, Switzerland). Cell viability was normalized to that of 786-O cells cultured in the complete culture medium without the incubation with AuNPRs-MBA.

A.9 MATLAB Processing

The SERS data from the Raman microscope was outputted as a text file with four columns. The columns, in order, were: the X-axis coordinate of the scan location, the Y-axis coordinate of the scan location, the wavelength being measured, and the SERS intensity at the given location and wavelength. This data was imported to MATLAB, where a custom program averaged the relevant data and trimmed the unnecessary data, leaving SERS intensity at 1079 cm^{-1} and 1394 cm^{-1} for each scan location. Background subtraction was performed by calculating two baselines (one for each wavelength position) that were subtracted from the SERS intensity value. The data was then rearranged to populate a matrix of $m \times n$ dimension, where m represents the number of distinct Y coordinates and n represents the number of distinct X coordinates. By converting the absolute coordinates to corresponding matrix cells, we were able to use the $imagesc$ command to generate a colormap of intensity.

To calculate the pH of the pixels within the cell, we first had to delineate between pixels that represented a location within the cell and pixels that represented a location outside the cell. To do this, we imported the dark field cell image to ImageJ and split the image to its RGB channel components. From there, the red channel was selected (the others were discarded) and that image was converted to a binary image. We specified a length scale according to the scale bar on the original dark field image, and we used the $Analyze\ Particles$ feature to calculate the area of the cell. This value was then divided by the area of each pixel, which was determined by the step size in the coordinates, yielding the number of pixels that the cell was split into. Making the assumption that the pixels in the cell had higher SERS intensity than the pixels outside the cell, we kept only the highest SERS intensity pixels to create the cell image. From the remaining pixels, we calculated the ratio between 1394 cm^{-1} and 1079 cm^{-1} and obtained the corresponding pH value from our calibration curve (Fig. 4.1B). Because our calibration curve only reached pH 5, any ratio below the ratio corresponding to pH 5 was assigned a pH value of 5.

Appendix B

Synthesis Methods

B.1 Materials

Unless otherwise specified, all the chemicals were purchased and used without further purification. Cetyltrimethylammonium bromide (CTAB), chloroauric acid, ascorbic acid, sodium borohydride, poly(styrene sulfonate) (PSS) (Mw=70,000 g/mol), poly(allyl amine hydrochloride) (PAH) (Mw=56,000 g/mol), poly-L-histidine hydrochloride (Mw>5,000 g/mol), sodium hydroxide (NaOH), mercaptobenzoic acid (MBA), penicillin/streptomycin, and G418 sulfate were purchased from Sigma-Aldrich. Silver nitrate and Lonza RPMI-1640 with 25 mM HEPES and L-Glutamine was purchased from VWR international. Methoxy PEG thiol (SH-PEG, Mw=5,000 g/mol) was purchased from Jenkem Technology. Phosphate and acetate buffer from pH 5.0 to 9.0 were purchased from G-Biosciences. Human renal cancer cell line (786-O) and Renal Proximal Tubule Cells (RPTEC) were purchased from ATCC (Manassas, VA). Fetal bovine serum (FBS), Trypsin-EDTA (0.25%), and Dulbecco's Phosphate-Buffered Saline (DPBS) were purchased from Life Technologies.

B.2 AuNR for Refractive Index Sensitivity

Gold nanorods were synthesized using a seed-mediated approach. [34, 35] Seed solution was prepared by adding 1mL of an ice-cold solution of 10 mM sodium borohydride into 10 mL of magnetically stirred 0.1 M CTAB and 2.5×10^{-4} M $HAuCl_4$ aqueous solution at room temperature. The color of the seed solution changed from yellow to brown. Growth solution was prepared by mixing 95 mL of 0.1 M CTAB, 0.8 mL of 10 mM silver nitrate, 5 mL of 10 mM $HAuCl_4$, and 0.55 mL of 0.1 M ascorbic acid in the same order. The solution was homogenized by gentle stirring. To the resulting colorless solution, 0.12 mL of freshly prepared seed solution was added and set aside in dark for 14 h. The solution turned from colorless to greenish brown, with most of the color change happening in the first hour. Prior to use, the gold nanorod solution was centrifuged at 13,000 rpm for 10 min to remove excess CTAB and redispersed in nanopure water (18.2 MΩ-cm). The centrifugation procedure was repeated twice.

B.3 Synthesis of AuNR for AuNPR

AuNRs were synthesized using a seed-mediated approach. [77, 78, 79] Seed solution was prepared by adding 0.6 ml of an ice-cold sodium borohydride solution (10 mM) to 10 ml of 0.1 M CTAB and 2.5 X 10^{-4} M $HAuCl_4$ solution under vigorous stirring at room temperature. The color of the seed solution changed from yellow to brown. Growth solution was prepared by mixing 100 ml of CTAB (0.1 M), 5 ml of $HAuCl_4$ (10 mM), 1.0 ml of silver nitrate (10 mM), 0.8 ml of ascorbic acid (0.1 M) and 1 ml of HCl (1M) consecutively. The solution was homogenized by gentle stirring. To the resulting colorless solution, 0.24 ml of freshly prepared seed solution was added and set aside in the dark for 14 h.

B.4 Synthesis and Surface Modifications of AuNPRs

AuNPRs were synthesized by employing AuNRs as cores. First, 100 µl of aqueous poly-L-histidine (poly-his) solution (5 mg/ml) was added to 1 ml of PSS coated AuNRs (concentration adjusted to realize an extinction intensity of 2.0) followed by brief vortexing and incubation for 10 min. After centrifugation at 7,000 rpm for 10 min, the pellet was dispersed in nanopure water (18.2MΩ-cm). Immediately, 30 µl of aqueous $HAuCl_4$ solution (20 mM) was added to the above solution, followed by adjusting the pH of the reaction solution to 6.4 by the addition of 28 µl of aqueous NaOH solution (100 mM). After 3 min, 20 µl of aqueous ascorbic acid solution (1 M) and 200 µl of aqueous polyvinylpyrrolidone solution (90 mM) were added as a reducing agent and capping agent, respectively. Different amounts of $HAuCl_4$ (5-60 µl) were used to control the packing density of clusters grown on AuNR template. To 1 ml of once-centrifuged AuNPRs, 80 µl of 2 mM methoxy polyethylene glycol thiol (SH-PEG) aqueous solution and 6 µl of 10 mM pMBA ethanol solution were added subsequently. After 1 h shaking, the above solution was centrifuged and dispersed in phosphate and acetate buffer from pH 5.0 to 9.0 to calibrate the intensity ratio of Raman bands 1394 cm^{-1} /1079 cm^{-1} as a function of pH. The centrifuged PEGlated AuNPRs-pMBA were also dispersed in RPMI-1640 medium with 10% FBS for cellular experiments. Similarly, AuNPSs were synthesized by using 10 µl of 20 mM $HAuCl_4$ to 1 ml of PSS coated AuNPs with extinction 1.0.

B.5 Synthesis of AuNS

AuNSs were synthesized using a seed-mediated method reported previously with slight modifications. A seed solution was prepared by vigorous mixing of 9.5 ml of aqueous cetyltrimethylammonium chloride (CTAC) solution (0.1 M) and 515 µl of aqueous HAuCl4 solution (4.86 mM), with 450 µl of ice-cold $NaBH_4$. The seed solution was aged for 1 h at 30 °C in a hot bath. In the next step, growth solution was prepared by mixing 9.5 mL of aqueous CTAC solution (0.1 M), 515 µl of aqueous $HAuCl_4$ solution (4.86 mM), and 150 µl of ascorbic acid (0.04 M). To this colorless solution, 25 µl of seed was added with vigorous stirring and kept undisturbed for two days to obtain highly uniform spherical nanoparticles with LSPR peak at 530 nm. The shape and uniformity of the nanoparticles were verified by TEM.

Appendix C

Supporting Information

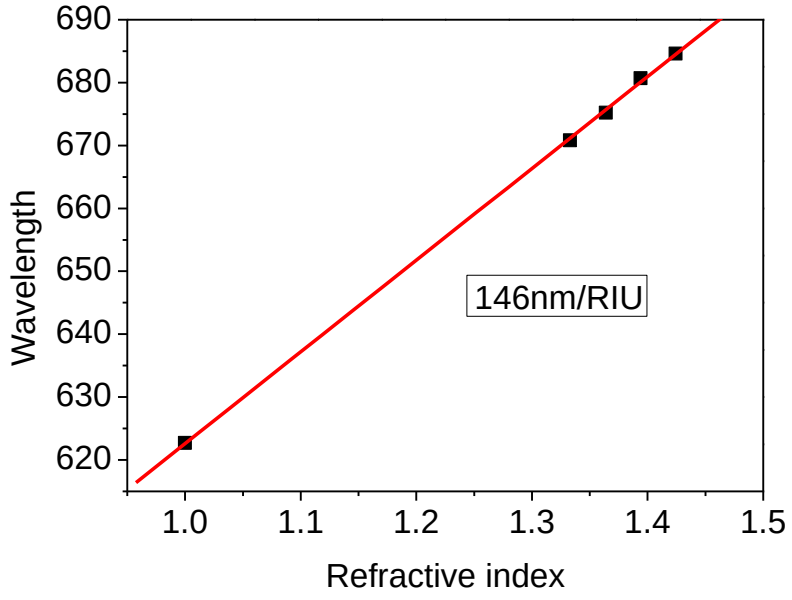

Figure S.1 - Refractive index sensitivity of AuNRs measured on a glass substrate. The solvents with different refractive index are air, H2O, and 20%, 37%, 52% (w/v) sucrose solution.

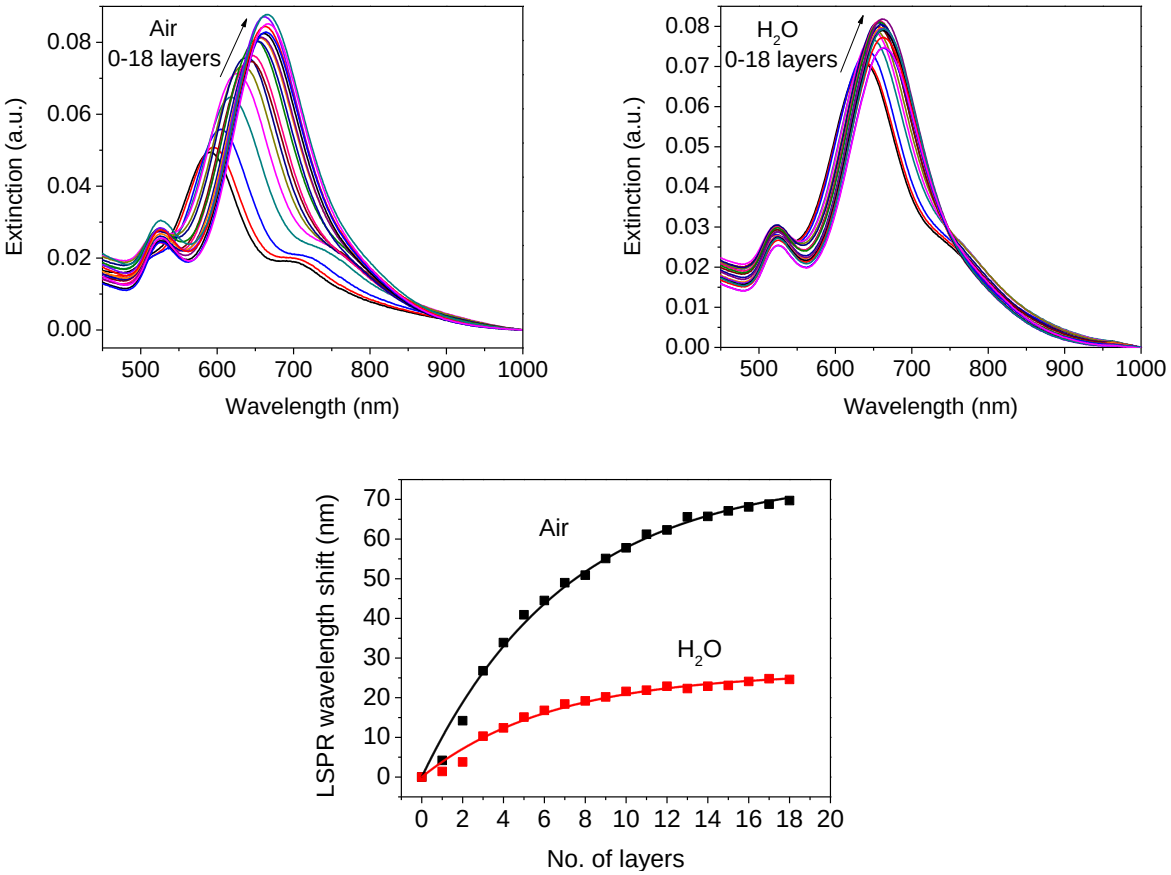

Figure S.2 - Extinction spectra of AuNR collected in air and H_2O after the deposition of each polyelectrolyte layer, and cumulative LSPR shift of the longitudinal plasmon band of the AuNR with the number of bilayers. The percent swelling was calculated to be 20% using the AuNR with aspect ratio 2.3. The results showed the same swelling percentage of PEM was obtained by using AuNRs with different aspect ratio within deviation range.

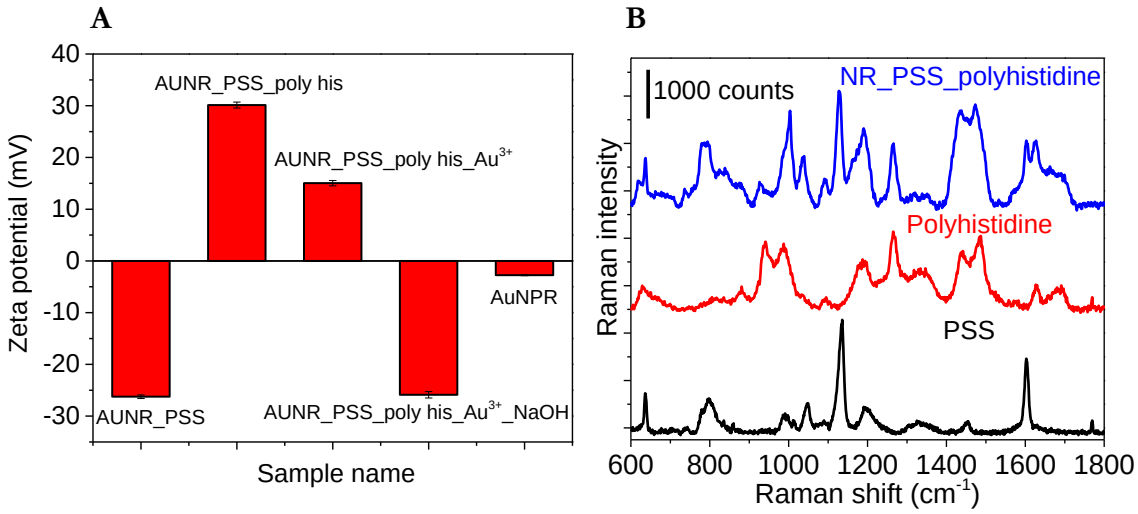

Figure S.3 - (A) Zeta potential following each step of AuNPR synthesis (B) Raman spectra of AuNR modified with PSS and poly-L-histidine, and bulk form of PSS and poly-L-histidine.

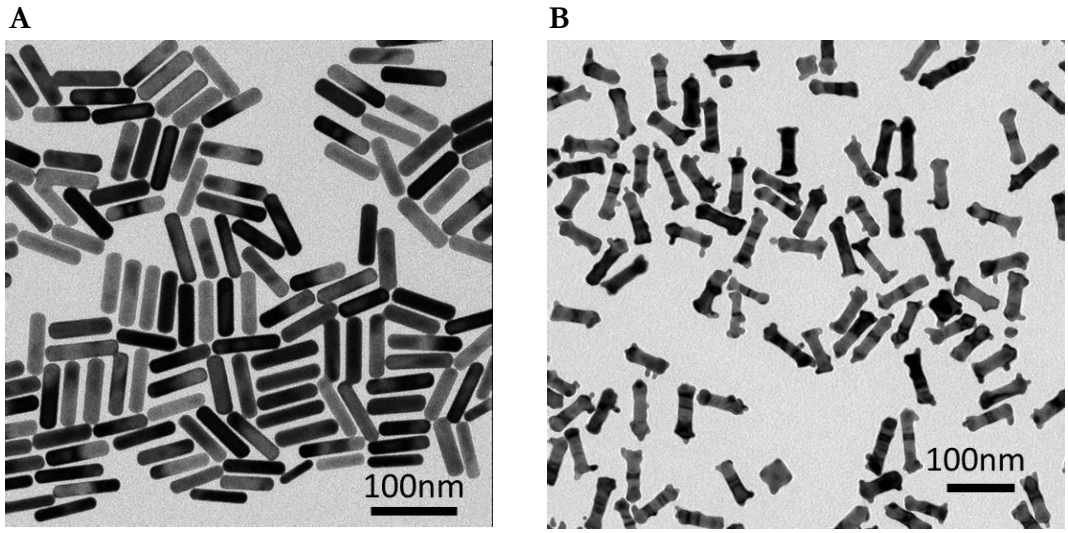

Figure S.4 - TEM images of (A) AuNR. (B) AuNPRs synthesized by adding 10 µl of HAuCl4 without poly-his addition.

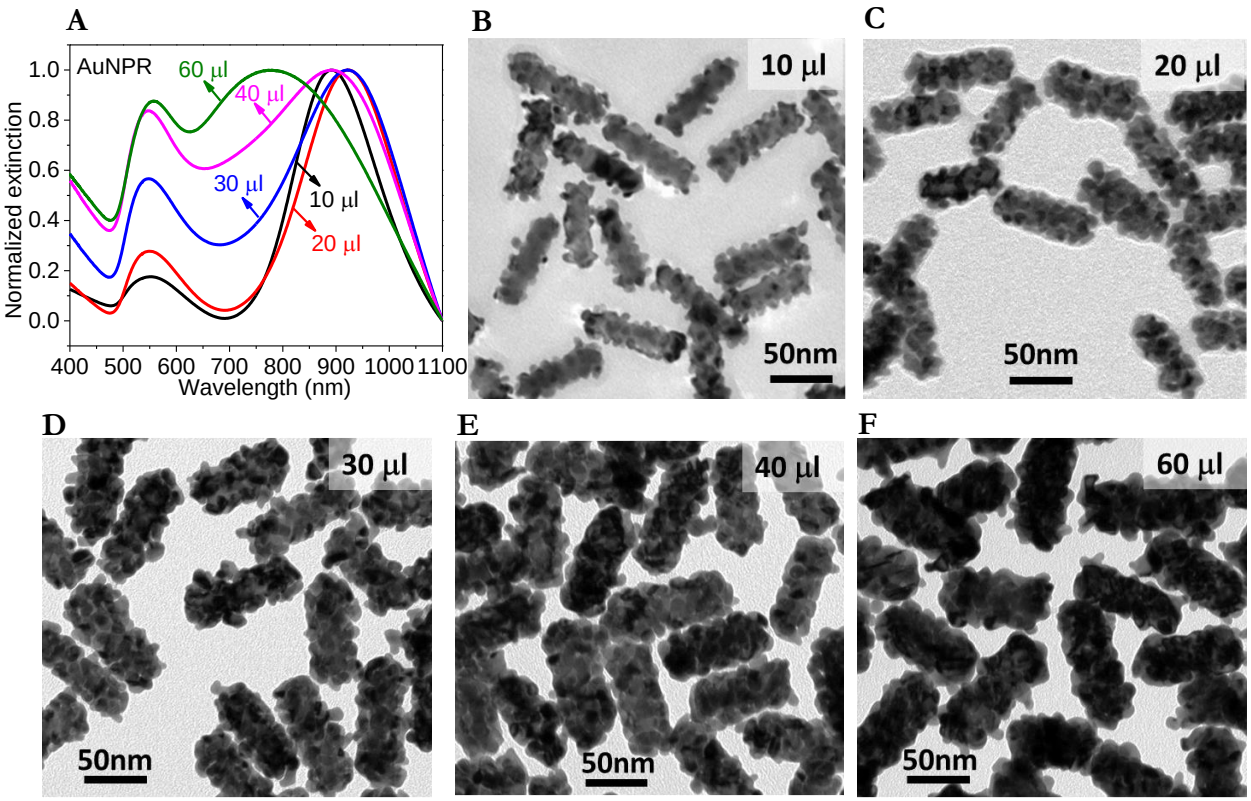

Figure S.5 - (A) Extinction spectra and corresponding TEM images of AuNPRs synthesized by adding (B) 10 µl (C) 20 µl (D) 30 µl (E) 40 µl (F) 60 µl $HAuCl_4$ precursor.

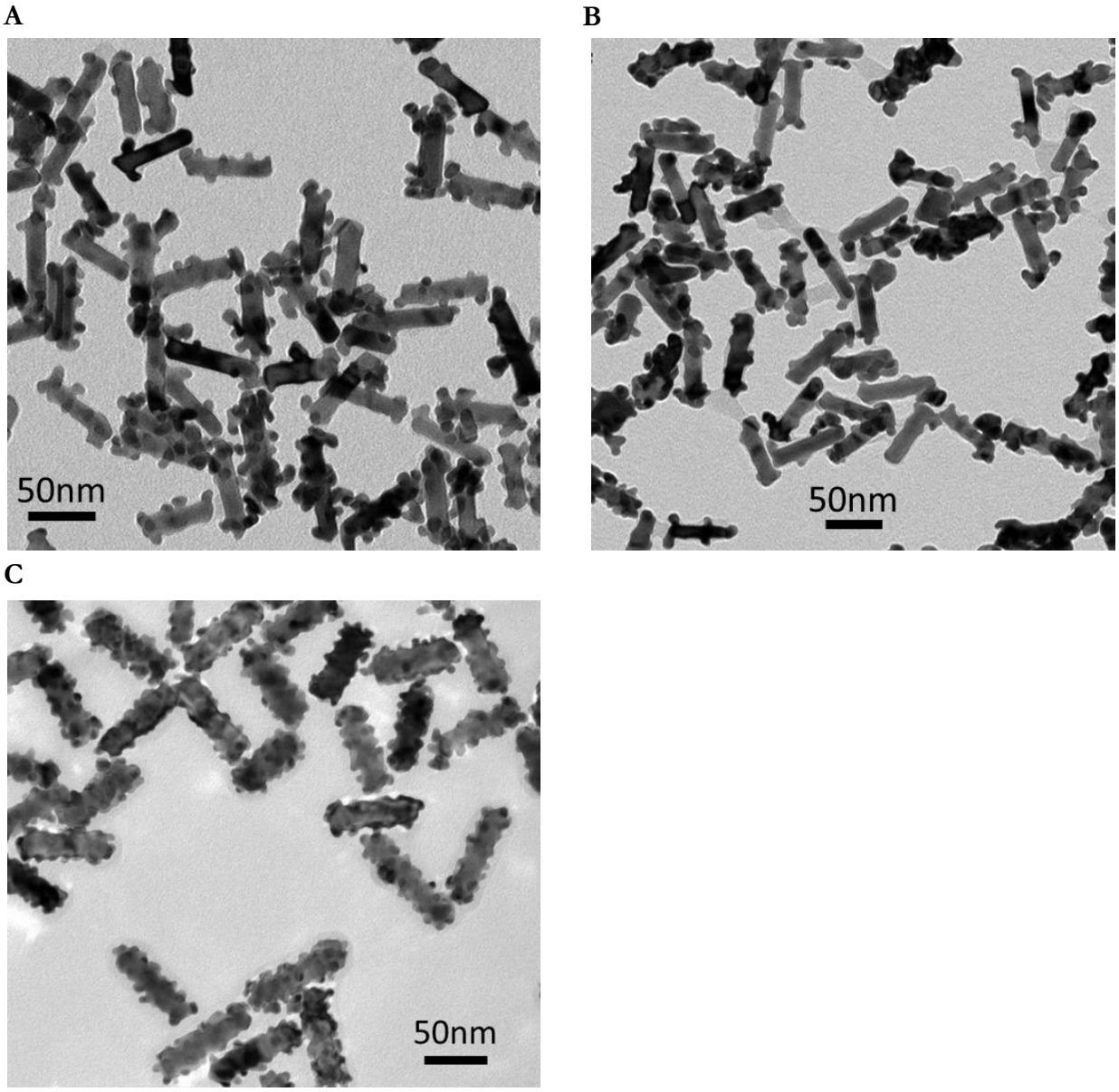

Figure S.6 - Control experiments demonstrating the effect of pH on the formation of satellites on AuNR cores. TEM images of the resultant nanostructures with the addition of (A) 5 μl of 1M HCl to achieve the reaction at pH 2 (B) Without HCl or NaOH to achieve the reaction at pH 3.4 (C) 5 μl of 0.1 M NaOH to achieve the reaction at pH 6.4.

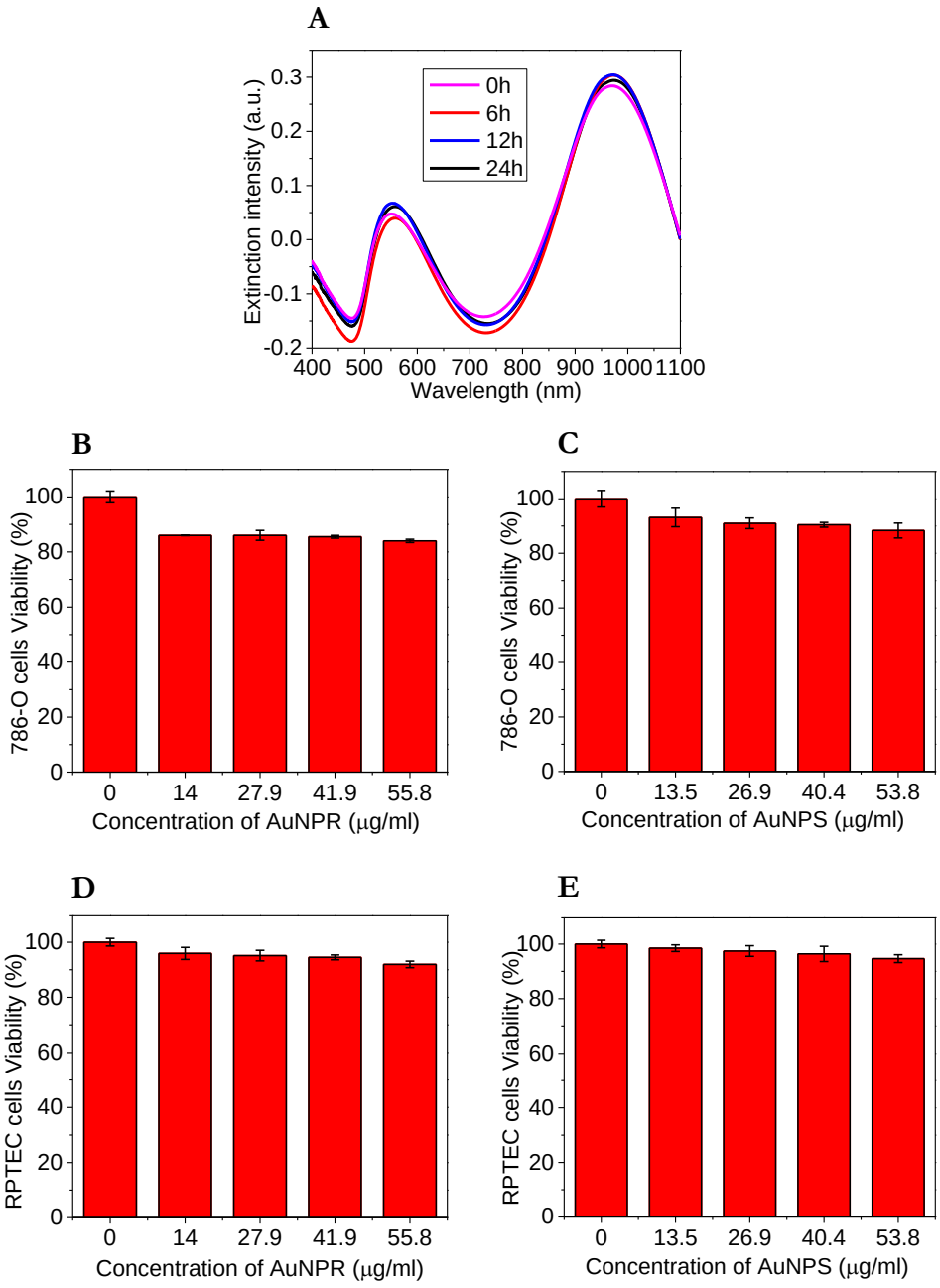

Figure S.7 - (A) Extinction spectra of AuNPR dispersed in 10% fetal bovine serum (FBS) at different time points showing the remarkable stability of the nanostructures in complex biological milieu. Viability of human renal adenocarcinoma cells (786-O) incubated with (B) AuNPR-pMBA and (C) AuNPS-pMBA at different concentrations of Au atoms showing the minimal toxicity. Viability of renal primary proximal tubule epithelial cells (RPTEC) incubated with (D) AuNPR-pMBA and (E) AuNPS-pMBA showing the minimal toxicity.

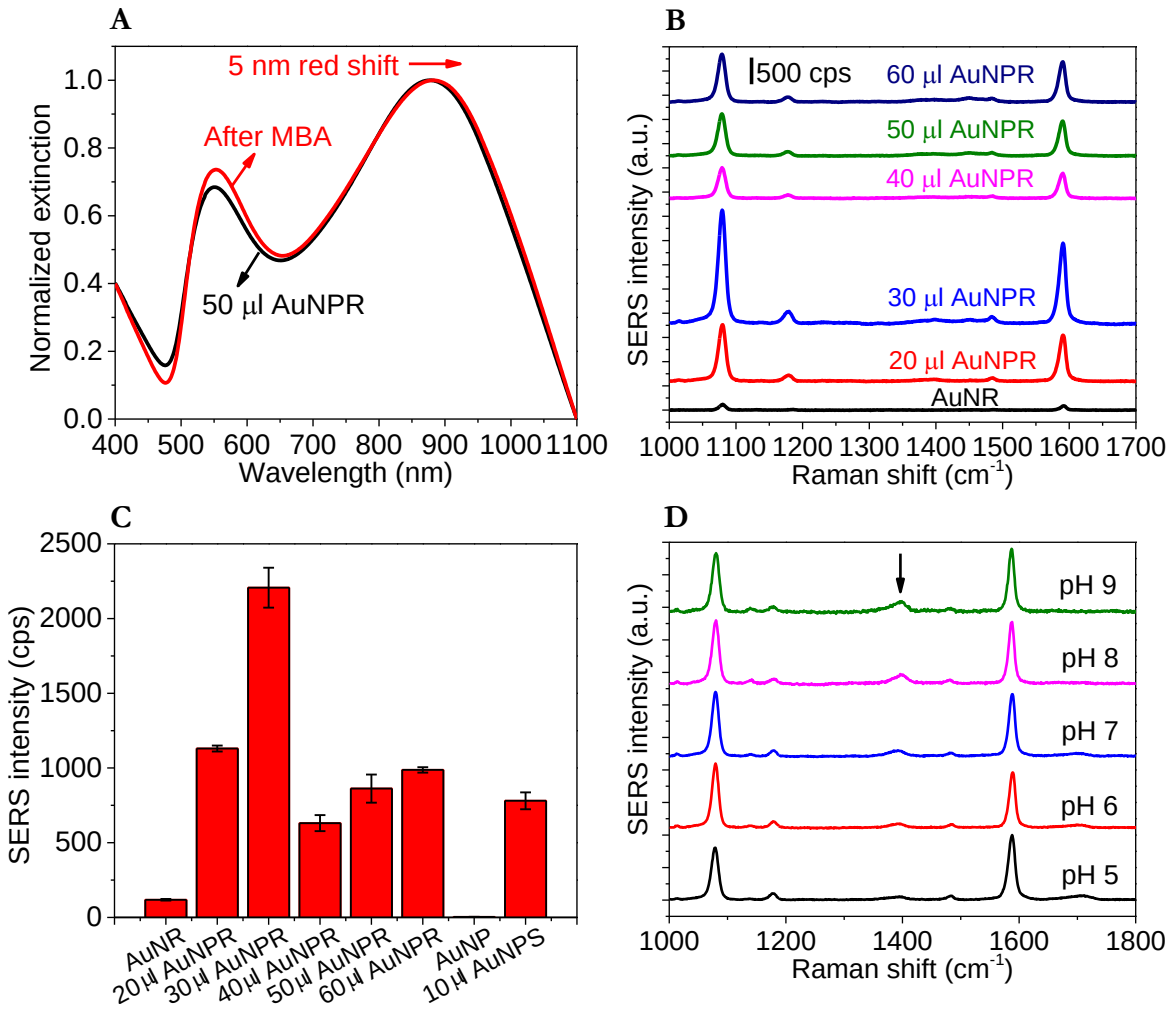

Figure S.8 - (A) Extinction spectra of AuNPR before and after chemisorption of pMBA showing a 5 nm red shift in the longitudinal LSPR wavelength upon adsorption of pMBA. (B) SERS spectra obtained from AuNPR synthesized by adding different amounts of $HAuCl_4$ precursor (corresponding TEM images shown in Fig. S.3) (C) Histogram showing the intensity of 1079 cm^{-1} Raman band for AuNR, AuNPRs synthesized with addition of differing amounts of Au precursor. (D) Representative SERS spectra from AuNPR at pH 5 to 9, showing the relative Raman intensity increase of the symmetric carboxylate stretching band of pMBA at 1394 cm^{-1} with respect to 1079 cm^{-1} with increasing pH due to the deprotonation of the carboxylate group.

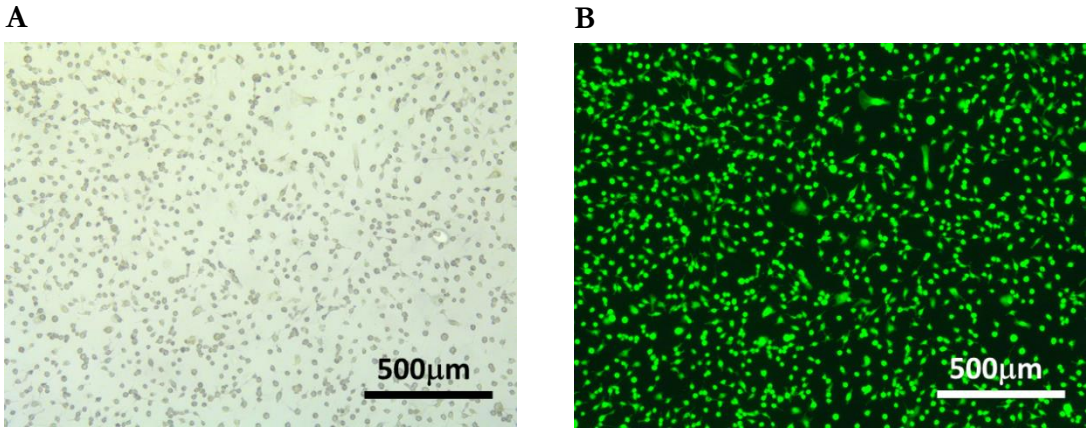

Figure S.9 - Bright field (A), green fluorescence (indicating live cells) (B) images of cells incubated with AuNPR to ensure the viability of cells after the living cell imaging.

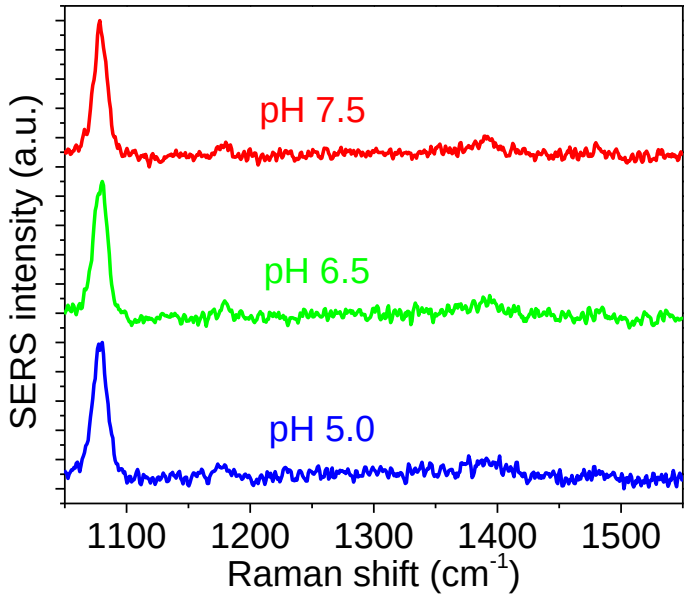

Figure S.10 - Representative spectra at different pH depicted as color-coded pixels using MATLAB.

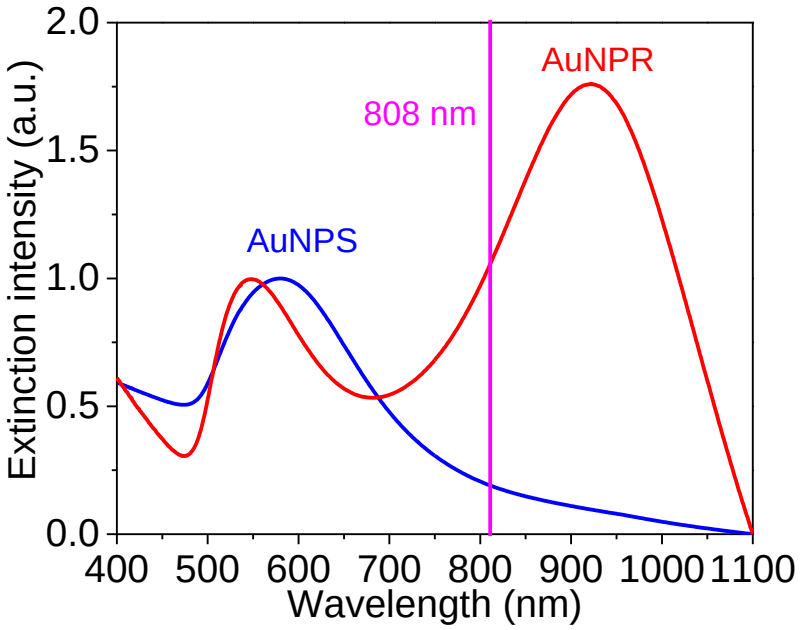

Figure S.11 - Extinction spectra of AuNPR and AuNPS solution at the similar concentration of ~55 µg/ml Au atoms.

References

[1] N. Gandra, L. Tian, S. Z. Nergiz and S. Singamaneni, "Migration of plasmonics from static to dynamic surfaces," *J. Nanosci. Lett.,* vol. 4, no. 23, 2014.

[2] C. H. Lee, M. E. Hankus, L. Tian, P. M. Pellegrino and S. Singamaneni, "Highly Sensitive Surface Enhanced Raman Scattering Substrates Based on Filter Paper Loaded with Plasmonic Nanostructures," *Anal. Chem.,* vol. 83, no. 23, 2011.

[3] K. M. Mayer and J. H. Hafner, "Localized Surface Plasmon Resonance Sensors," *Chem. Rev.,* vol. 111, p. 3828, 2011.

[4] J. N. Anker, W. P. Hall, O. Lyandres, N. C. Shah, J. Zhao and R. P. Van Duyne, "Biosensing with plasmonic nanosensors," *Nature Mater.,* vol. 7, p. 442, 2008.

[5] B. Sepulveda, A. P. C, L. M. Lechuga and L. M. Liz-Marzan, "LSPR-based nanobiosensors," *Nano Today,* vol. 4, p. 244, 2009.

[6] A. J. Haes and R. P. Van Duyne, "A Nanoscale Optical Biosensor: Sensitivity and Selectivity of an Approach Based on the Localized Surface Plasmon Resonance Spectroscopy of Triangular Silver Nanoparticles," *J. Am. Chem. Soc.,* vol. 10596, p. 124, 2002.

[7] J. C. Riboh, A. J. Haes, A. D. McFarland, C. R. Yonzon and R. P. Van Duyne, "A Nanoscale Optical Biosensor: Real-Time Immunoassay in Physiological Buffer Enabled by Improved Nanoparticle Adhesion," *J. Phys. Chem. B,* vol. 107, p. 1772, 2003.

[8] C. R. Yonzon, E. Jeoung, S. Zou, G. C. Schatz, M. Mrksich and R. P. Van Duyne, "A Comparative Analysis of Localized and Propagating Surface Plasmon Resonance Sensors: The Binding of Concanavalin A to a Monosaccharide Functionalized Self-Assembled Monolayer," *J. Am. Chem. Soc.,* vol. 126, p. 12669, 2004.

[9] A. J. Haes, L. Chang, W. L. Klein and R. P. Van Duyne, "Detection of a Biomarker for Alzheimer's Disease from Synthetic and Clinical Samples Using a Nanoscale Optical Biosensor," *J. Am. Chem. Soc.,* vol. 127, p. 2264, 2005.

[10] J. M. Bingam, J. N. Anker, L. E. Kreno and R. P. Van Duyne, "Gas sensing with high-resolution localized surface plasmon resonance spectroscopy," *J. Am. Chem. Soc.,* vol. 132, p. 17358, 2005.

[11] W. P. Hall, J. Modic, J. Anker, Y. Lin, M. Mrksich and R. P. Van Duyne, "A Conformation- and Ion-Sensitive Plasmonic Biosensor," *Nano Lett.,* vol. 11, p. 1098, 2011.

[12] C. Novo, A. M. Funston, A. K. Gooding and P. Mulvaney, "Electrochemical Charging of Single Gold Nanorods," *J. Am. Chem. Soc.,* vol. 131, p. 14664, 2009.

[13] C. Novo, A. M. Funston and M. P, "Direct observation of chemical reactions on single gold nanocrystals using surface plasmon spectroscopy," *Nat. Nanotechnol.,* vol. 3, p. 598, 2008.

[14] I. Tokarev, I. Tokareva and S. Minko, "Optical Nanosensor Platform Operating in Near-Physiological pH Range via Polymer-Brush-Mediated Plasmon Coupling," *ACS Appl. Mater. Interfaces,* vol. 3, p. 143, 2011.

[15] H. Kitano, H. Kago and K. Matsuura, "Temperature-responsive polymer brush constructed on a colloidal gold monolayer," *J. Colloid Interface Sci.,* vol. 331, p. 343, 2009.

[16] M. Mitsuishi, Y. Koishikawa, H. Tanak, E. Sato, T. Mikayama, J. Matsui and T. Miyashita, "Nanoscale Actuation of Thermoreversible Polymer Brushes Coupled with Localized Surface Plasmon Resonance of Gold Nanoparticles," *Langmuir,* vol. 23, p. 7472, 2007.

[17] S. Kima, N. Chenga, J. Jeongb, J. S, Y. S and W. T. S. Huck, "Localized surface plasmon resonance (LSPR) sensitivity of Au nanodot patterns to probe solvation effects in polyelectrolyte brushes," *Chem. Commun.,* vol. 31, p. 3666, 2008.

[18] S. Z. Nergiz and S. Singamaneni, "Reversible Tuning of Plasmon Coupling in Gold Nanoparticle Chains Using Ultrathin Responsive Polymer Film," *ACS Appl. Mater. Interfaces,* vol. 3, p. 945, 2011.

[19] V. Kozlovskaya, E. Kharlampieva, B. P. Khanal, P. Manna, E. R. Zubarev and V. V. Tsukruk, "Ultrathin Layer-by-Layer Hydrogels with Incorporated Gold Nanorods as pH-Sensitive Optical Materials," *Chem. Mater.,* vol. 20, p. 7474, 2008.

[20] C. Langhammer, E. M. Larsson, B. Kasemo and I. Zoric, "Indirect Nanoplasmonic Sensing: Ultrasensitive Experimental Platform for Nanomaterials Science and Optical Nanocalorimetry," *Nano Lett.,* vol. 10, p. 3529, 2010.

[21] G. Decher, "Fuzzy Nanoassemblies: Toward Layered Polymeric Multicomposites," *Science,* vol. 277, p. 1232, 1997.

[22] J. Park, L. D. Fouche and P. T. Hammond, "Multicomponent Patterning of Layer-by-Layer Assembled Polyelectrolyte/Nanoparticle Composite Thin Films with Controlled Alignment," *Adv. Mater.,* vol. 2575, p. 17, 2005.

[23] S. T. Dubas and J. B. Schlenoff, "Swelling and Smoothing of Polyelectrolyte Multilayers by Salt," *Langmuir,* vol. 17, p. 7725, 2001.

[24] A. A. Antipov, G. B. Sukhorukov and H. Mohwald, "Influence of the Ionic Strength on the Polyelectrolyte Multilayers' Permeability," *Langmuir,* vol. 19, p. 2444, 2003.

[25] R. Steitz, V. Leiner, K. Tauer, V. Khrenov and R. V. Klitzing, "Temperature-induced changes in polyelectrolyte films at the solid–liquid interface," *aPPL. pHYS. a,* vol. 74, p. s519, 2002.

[26] E. Kharlampieva, V. Kozlovskaya, J. Chan, J. F. Ankner and V. V. Tsukruk, "Spin-assisted layer-by-layer assembly: variation of stratification as studied with neutron reflectivity," *Langmuir,* vol. 25, p. 14017, 2009.

[27] K. E. Achyuthan, T. S. Bergstedt, L. Chen, R. M. Jones, S. Kumaraswamy, S. A. Kushon, K. D. Ley, L. Lu, D. McBranch, H. Mukundan, F. Rininsland, X. Shi, W. Xia and D. G. Whitten, "Fluorescence superquenching of conjugated polyelectrolytes: applications for biosensing and drug discovery," *J. Mater. Chem.,* vol. 15, p. 2648, 2005.

[28] X. Wang, B. Ding, J. Yu, M. Whang and F. Pan, "A highly sensitive humidity sensor based on a nanofibrous membrane coated quartz crystal microbalance," *Nanotechnology,* vol. 21, p. 055502, 2010.

[29] O. Kedem, A. B. Tesler, A. Vaskevich and I. Rubinstein, "Sensitivity and Optimization of Localized Surface Plasmon Resonance Transducers," *ACS Nano,* vol. 5, p. 748, 2011.

[30] J. E. Wong, F. Rehfeldt, P. Hanni, M. Tanaka and R. V. Klitzing, "Swelling Behavior of Polyelectrolyte Multilayers in Saturated Water Vapor," *Macromolecules,* vol. 37, p. 7285, 2004.

[31] O. M. Tanchak and C. J. Barrett, "Correlation of the Swelling and Permeability of Polyelectrolyte Multilayer Films," *Chem. Mater.,* vol. 16, p. 2734, 2004.

[32] M. D. Miller and M. L. Bruening, "Correlation of the Swelling and Permeability of Polyelectrolyte Multilayer Films," *Chem. Mater.,* vol. 17, p. 5375, 2005.

[33] M. Svedendahl, S. Chen, A. Dmitriev and M. Kall, "Refractometric sensing using propagating versus localized surface plasmons: a direct comparison," *Nano Lett.,* vol. 9, p. 4428, 2009.

[34] K. S. Lee and M. A. El-Sayed, "Dependence of the Enhanced Optical Scattering Efficiency Relative to That of Absorption for Gold Metal Nanorods on Aspect Ratio, Size, End-Cap Shape, and Medium Refractive Index," *J. Phys. Chem. B,* vol. 109, p. 20331, 2005.

[35] A. Gole and C. J. Murphy, "Azide-Derivatized Gold Nanorods: Functional Materials for "Click" Chemistry," *Langmuir,* vol. 24, p. 266, 2008.

[36] S. Malynych, I. Luzinov and G. Chumanov, "Poly(Vinyl Pyridine) as a Universal Surface Modifier for Immobilization of Nanoparticles," *J. Phys. Chem. B,* vol. 106, p. 1280, 2002.

[37] P. K. Jain and M. A. El-Sayed, "Noble Metal Nanoparticle Pairs: Effect of Medium for Enhanced Nanosensing," *Nano Lett.,* vol. 8, p. 4347, 2008.

[38] F. Caruso, K. Niikura, D. N. Furlong and Y. Okahata, "Ultrathin Multilayer Polyelectrolyte Films on Gold: Construction and Thickness Determination," *Langmuir,* vol. 13, p. 3422, 1997.

[39] J. Cho, H. Jang, B. Yeom, H. Kim, R. Kim, S. Kim and K. Char, "Modulating the Pattern Quality of Micropatterned Multilayer Films Prepared by Layer-by-Layer Self-Assembly," *Langmuir,* vol. 22, p. 1356, 2006.

[40] H. Jang, S. Kim and K. Char, "Multilayer line micropatterning using convective self-assembly in microfluidic channels," *Langmuir,* vol. 19, p. 3094, 2003.

[41] C. Jiang, S. Markutsya and V. V. Tsukruk, "Collective and Individual Plasmon Resonances in Nanoparticle Films Obtained by Spin-Assisted Layer-by-Layer Assembly," *Langmuir,* vol. 20, p. 882, 2004.

[42] C. Jiang, S. Singamaneni, E. Merrick and V. V. Tsukruk, "Complex Buckling Instability Patterns of Nanomembranes with Encapsulated Gold Nanoparticle Arrays," *Nano Lett.,* vol. 6, p. 2254, 2006.

[43] K. H, C. Jiang, H. Shulha and V. V. Tsukruk, "Carbon nanotube arrays encapsulated into freely suspended flexible films," *Chem. Mater.,* vol. 17, p. 2490, 2005.

[44] R. Gunawidjaja, C. Jiang, S. Peleshanko, M. Ornatska, S. Singamaneni and V. V. Tsukruk, "Flexible and Robust 2D Arrays of Silver Nanowires Encapsulated within Freestanding Layer-by-Layer Films," *Adv. Funct. Mat.,* vol. 16, p. 2024, 2006.

[45] M. D. Malinsky, K. L. Kelly, G. C. Schatz and R. P. Van Duyne, "Chain Length Dependence and Sensing Capabilities of the Localized Surface Plasmon Resonance of Silver Nanoparticles

Chemically Modified with Alkanethiol Self-Assembled Monolayers," *J. Am. Chem. Soc.,* vol. 123, p. 1471, 2001.

[46] M. Garnet, "Colours in Metal Glasses and in Metallic Films," *Philos. Trans. R. Soc. London, Ser. A,* vol. 203, p. 385, 1904.

[47] M. Garnet, "Colours in metal glasses, in metallic films, and in metallic solutions," *Philos. Trans. R. Soc. London, Ser. A,* vol. 205, p. 237, 1906.

[48] J. Vesna, S. Jordi and Z. Hrvoje, "Refractive index profile modelling of dielectric inhomogeneous coatings using effective medium theories," *Thin Solid Films,* vol. 516, p. 3368, 2008.

[49] M. F. Kircher, A. de la Zerda, J. V. Jokerst, C. L. Zavaleta, P. J. Kempen, E. Mittra, K. Pitter, R. Huang, C. Campos, F. Habte, R. Sinclair, C. W. Brennan, I. K. Mellinghoff, E. C. Holland and S. S. Gambhir, "A brain tumor molecular imaging strategy using a new triple-modality MRI-photoacoustic-Raman nanoparticle," *Nat. Med.,* vol. 18, p. 829, 2012.

[50] X. Qian, X. H. Peng, D. O. Ansari, Q. Yin-Goen, G. Z. Chen, D. M. Shin, L. Yang, A. N. Young, M. D. Wang and S. Nie, "In vivo tumor targeting and spectroscopic detection with surface-enhanced Raman nanoparticle tags," *Nat. Biotech.,* vol. 26, p. 83, 2008.

[51] C. L. Zavaleta, E. Garai, J. T. C. Liu, S. Sensarn, M. J. Mandella, D. Van de Sompel, S. Friedland, J. Van Dam, C. H. Contag and S. S. Gambhir, "Multiplexed imaging of surface enhanced Raman scattering nanotags in living mice using noninvasive Raman spectroscopy," *P. Natl. Acad. Sci. USA,* vol. 110, p. 10062, 2013.

[52] S. Nie and S. R. Emory, "Probing single molecules and single nanoparticles by surface-enhanced raman scattering," *Science,* vol. 275, p. 1102, 1997.

[53] B. E. Riddell, R. J. Beamish, L. J. Richards and J. R. Candy, "Comment on "Declining Wild Salmon Populations in Relation to Parasites from Farm Salmon"," *Science,* vol. 322, p. 1790, 2008.

[54] N. Gandra and S. Singamaneni, "Bilayered Raman-Intense Gold Nanostructures with Hidden Tags (BRIGHTs) for High-Resolution Bioimaging," *Advanced Materials,* vol. 25, p. 1022, 2013.

[55] D. K. Lim, K. S. Jeon, J. H. Hwang, H. Kim, S. Kwon, Y. D. Suh and J. M. Nam, "Highly uniform and reproducible surface-enhanced Raman scattering from DNA-tailorable nanoparticles with 1-nm interior gap," *Nat. Nano.,* vol. 6, p. 452, 2011.

[56] M. Yang, R. N. Alvarez-Puebla, H. S. Kim, P. Aldeanueva-Potel, L. M. Liz-Marzan and N. A. Kotov, "SERS-Active Gold Lace Nanoshells with Built-in Hotspots," *Nano. Lett.,* vol. 10, p. 4013, 2010.

[57] R. Djaalali, Y. F. Chen and H. Matsui, "Au Nanocrystal Growth on Nanotubes Controlled by Conformations and Charges of Sequenced Peptide Templates," *J. Am. Chem. Soc.,* vol. 125, p. 5873, 2003.

[58] Y. Jin and X. Gao, "Plasmonic fluorescent quantum dots," *Nat. Nano.,* vol. 4, p. 571, 2009.

[59] S. L. Klienman, B. Sharma, M. G. Blaber, A. I. Henry, N. Valley, R. G. Freeman, M. J. S. G. C. Natan and R. P. Van Duyne, "Structure Enhancement Factor Relationships in Single Gold Nanoantennas by Surface-Enhanced Raman Excitation Spectroscopy," *J. Am. Chem. Soc.,* vol. 135, p. 301, 2012.

[60] N. Gandra, A. Abbas, L. Tian and S. Singamaneni, "Plasmonic Planet–Satellite Analogues: Hierarchical Self-Assembly of Gold Nanostructures," *Nano Lett.,* vol. 12, p. 2645, 2012.

[61] W. Li, P. H. C. Camargo, X. Lu and Y. Xia, "Dimers of Silver Nanospheres: Facile Synthesis and Their Use as Hot Spots for Surface-Enhanced Raman Scattering," *Nano Lett.,* vol. 9, p. 485, 2008.

[62] S. Ohkuma and B. Poole, "Fluorescence probe measurement of the intralysosomal pH in living cells and the perturbation of pH by various agents," *P. Natl. Acad. Sci. USA,* vol. 75, p. 3327, 1978.

[63] O. Seksek and J. Bolard, "Nuclear pH gradient in mammalian cells revealed by laser microspectrofluorimetry," *J. Cell Sci.,* vol. 109, p. 257, 1996.

[64] G. Miesenbock, D. A. De Angelis and J. E. Rothman, "Visualizing secretion and synaptic transmission with pH-sensitive green fluorescent proteins," *Nature,* vol. 394, p. 192, 1998.

[65] V. T. Cong, E. O. Ganbold, J. K. Saha, J. Jang, J. Min, J. Choo, S. Kim, N. W. Song, S. J. Son, S. B. Lee and S. W. Joo, "Gold Nanoparticle Silica Nanopeapods," *J. Am. Chem. Soc.,* vol. 136, p. 3833, 2014.

[66] J. Kneipp, H. Kneipp, B. Wittig and K. Kneipp, "One- and Two-Photon Excited Optical pH Probing for Cells Using Surface-Enhanced Raman and Hyper-Raman Nanosensors," *Nano Lett.,* vol. 7, p. 2819, 2007.

[67] J. Kneipp, H. Kneipp, B. Wittig and K. Kneipp, "Following the Dynamics of pH in Endosomes of Live Cells with SERS Nanosensors," *J. Phys. Chem. C,* vol. 114, p. 7421, 2010.

[68] R. Duncan, "Polymer conjugates as anticancer nanomedicines," *Nat. Rev. Cancer,* vol. 6, p. 688, 2006.

[69] B. D. Chithrani, A. A. Ghazani and W. C. W. Chan, "Determining the Size and Shape Dependence of Gold Nanoparticle Uptake into Mammalian Cells," *Nano Lett.,* vol. 6, p. 662, 2006.

[70] D. Hofmann, S. Tenzer, M. B. Bannwarth, C. Messerschmidt, S. F. Glaser, H. Schild, K. Landfester and V. Mailander, "Mass spectrometry and imaging analysis of nanoparticle-containing vesicles provide a mechanistic insight into cellular trafficking," *ACS Nano,* vol. 8, p. 10077, 2014.

[71] A. Sorkin and M. von Zastrow, "Endocytosis and signalling: intertwining molecular networks," *Nat. Rev. Mol. Cell Bio.,* vol. 3, p. 600, 2002.

[72] E. C. Cho, Q. Zhang and Y. Xia, "The effect of sedimentation and diffusion on cellular uptake of gold nanoparticles," *Nature Nano.,* vol. 6, p. 385, 2011.

[73] B. D. Chithrani and W. C. W. Chan, "Elucidating the Mechanism of Cellular Uptake and Removal of Protein-Coated Gold Nanoparticles of Different Sizes and Shapes," *Nano Letters,* vol. 7, p. 1542, 2007.

[74] S. Modi, M. G. Swetha, D. Goswami, G. D. Gupta, S. Mayor and Y. Krishnan, "A DNA nanomachine that maps spatial and temporal pH changes inside living cells," *Nature Nano,* vol. 4, p. 325, 2009.

[75] V. V. Tsukruk and S. Singamaneni, Scanning Probe Microscopy of Soft Matter: Fundamentals and Practices, Wiley-VCH, 2012.

[76] L. Pastoriza-Santos, J. Perez-Juste and L. M. Liz-Marzan, "Silica-Coating and Hydrophobation of CTAB-Stabilized Gold Nanorods," *Chem. Mater.,* vol. 18, p. 2465, 2006.

[77] N. R. Jana, L. Gearheart and C. J. Murphy, "Wet chemical synthesis of high aspect ratio cylindrical gold nanorods," *J. Phys. Chem. B,* vol. 105, p. 4065, 2001.

[78] B. Nikoobakht and M. A. El-Sayed, "Preparation and growth mechanism of gold nanorods using seed-mediated growth method," *Chem. Mater.,* vol. 15, p. 1957, 2003.

[79] J. Zhu, K. T. Yong, L. Roy, R. Hu, H. Ding, L. L. Zhao, M. T. Swihart, G. S. He, Y. P. Cui and P. N. Prasad, "Additive controlled synthesis of gold nanorods for two-photon luminescence imaging of cancer cells," *Nanotechnology,* p. 21, 2010.

Vita

Maximilian You Fei

Degrees	M.S. Materials Science and Engineering	May 2015
	B.S. Mechanical Engineering, *summa cum laude*	May 2014
Professional Experience	Quality Engineer, Boeing	Summer 2014
	Quality Engineer, SunEdison	Summer 2013
	Quality Engineer, SunEdison	Summer 2012

Publications

Bio-enabled Gold Superstructures with Built-in and Accessible Electromagnetic Hotspots. **2015**.

Externally-triggered Electromagnetic Hotspots through Spontaneous Folding of Plasmonic Gel. **2015**.

Plasmonic Nanorattles with Intrinsic Electromagnetic Hot-Spots for Surface Enhanced Raman Scattering. *Small*. **2014**.

Gold Nanorods as Nanotransducers to Monitor the Growth and Swelling of Ultrathin Polymer Films. *Nanotechnology*. **2012**.

Trapping Proteins Within Gold Nanoparticle Assemblies: Dynamically Tunable Hot-Spots for Nanobiosensing. *Plasmonics*. **2012**.